CHARACTERIZATION OF A TIE-LINE SERIES OF AUSTENITIC-FERRITIC STAINLESS STEELS

by

WILLIAM CHARLES MOFFATT

B.S., Massachusetts Institute of Technology

(1976)

Submitted in partial fulfillment of the requirements

for the degree of

MASTER OF SCIENCE

at the

Massachusetts Institute of Technology

September, 1978

Signature of Author .....
Department of Materials Science and Engineering
August 11, 1978

Certified by .....
Thesis Supervisor

Accepted by .....
Chairman, Departmental Committee on Graduate Students

ABSTRACT

CHARACTERIZATION OF A TIE-LINE SERIES OF

AUSTENITIC-FERRITIC STAINLESS STEELS

by

WILLIAM CHARLES MOFFATT

Submitted to the Department of Materials Science and Engineering on August 11, 1978, in partial fulfillment of the requirements for the Degree of Master of Science.

An experimental research program was conducted to determine some of the mechanical and physical properties of a tie-line series of austenitic-ferritic stainless steels. Rockwell B hardness tests and smooth bar bending fatigue tests were performed on these alloys at room temperature in laboratory air. The crystallographic textures, chemical compositions and microstructures of the phases present were also investigated.

Quantitative metallography of the microstructures showed progressive elongation and flattening of the phases, and a very small mean phase boundary intercept distance in alloys containing 61.4 v/o ferrite and 28.8 v/o ferrite. The true volume fractions of ferrite present in these alloys were found to be uniformly larger than those predicted from the ternary phase diagram.

Electron microprobe analyses of the alloys indicated that significant partitioning of the alloying elements between the austenite and ferrite phases occurred. Comparison of the observed phase compositions to those predicted from the ternary phase diagram suggests that the transformation of ferrite to austenite during processing may not have been completed.

Pole figure textural characterization of these steels showed pronounced intensity maxima aligned in the rolling direction. Overlap of the diffuse intensity ring associated with each maximum with other maxima brought about elongation of these intensity peaks in the transverse direction.

The Rockwell B hardness values showed a maximum for an alloy containing 61.4 v/o ferrite; the hardness values were found to correlate well with the tensile properties of the steels.

Smooth bar bending fatigue tests showed a maximum lifetime to occur for an alloy containing 90.7 v/o ferrite, and a maximum fatigue limit to occur for an alloy containing 61.4 v/o ferrite. The superior performance of these two alloys is thought to result from delayed crack initiation due to slip dispersal in the duplex alloys at low stress levels. At higher stresses the duplex microstructure likely mitigates against brittle crack propagation in the ferrite phase.

Thesis Supervisor: Regis M. Pelloux
Title: Professor of Materials Engineering

TABLE OF CONTENTS

TABLE OF CONTENTS (Cont'd.)

LIST OF FIGURES

LIST OF FIGURES (Cont'd.)

LIST OF TABLES

ACKNOWLEDGEMENTS

The author is grateful to a number of people and organizations for their assistance and encouragement during this study:

To Professor R. M. Pelloux, for his support and guidance throughout this investigation;

To Tateo Ohhashi and David Knorr, for their technical assistance during parts of the experimental program;

To the General Electric Corporate Research and Development Center, for providing the experimental alloys used in this investigation;

To the National Science Foundation, for financial support during the period of this study;

To Linda Sayegh, for typing the final manuscript;

and to the members of the High Temperature and Fatigue Research Group, for their support and camaraderie.

I. INTRODUCTION

In the quest for materials that can survive under high static and cyclic stresses in aggressive environments, austenitic-ferritic stainless steels, consisting of a fine mixture of a weak, ductile austenite phase and a strong brittle ferrite phase, have been developed. These alloys, also known as α-γ or duplex stainless steels, have been found to combine excellent corrosion resistance with good strength, ductility and fatigue resistance when produced in wrought form. As these steels minimize the problems associated with the parent phases (rapid failure by stress corrosion cracking in austenitic stainless steels and brittle crack propagation by cleavage in ferritic stainless steels), they have emerged as candidate materials for applications in the nuclear and chemical industries.

Five experimental alloys lying along a high temperature tie-line of the Fe-Ni-Cr ternary phase diagram were produced. This tie-line was chosen to include IN-744, an alloy produced by the International Nickel Company that has been well characterized in the literature. These alloys are expected to have invariant phase compositions; differences in behavior should then be related only to the varying volume fraction of ferrite.

Moskovitz [1] has considered the corrosion fatigue and fatigue crack propagation behavior of these alloys, and Hayden and Floreen [2, 3] have investigated their mechanical properties and fatigue performance. While some general aspects of the behavior of austenitic-ferritic stainless

steels are understood, many questions have remained unanswered. This thesis work was undertaken:

1. To assess the effect of hot rolling on the microstructures and crystallographic textures of the tie-line series alloys.
2. To relate the mechanical properties of these steels to their microstructures.
3. To determine the effect of the microstructures on the fatigue strengths of these alloys.

II. LITERATURE REVIEW

A. The Binary Phase Diagrams

Fe-Ni-Cr ternary alloys are, as a group, of considerable commercial interest and have received detailed attention from many investigators over the past several decades. An appreciation of the salient features of this phase equilibrium is a useful starting point for the study of microduplex stainless steels.

The binary phase diagrams Cr-Fe, Cr-Ni and Fe-Ni, serving as well characterized boundary conditions of the ternary equilibrium diagram, contribute much to our understanding of this system. They also introduce, in a simple setting, the phases that are of primary importance in determining the structure and physical properties of the ternary alloys. Excellent reviews of the literature of these three binary phase equilibria (through 1967) may be found in Hansen [4], Elliott [5] and Shunk [6]. The phase diagrams for these systems [7] appear in Figures 1, 2 and 3.

From the Fe-Ni phase diagram we find that FCC nickel is completely miscible with the ductile γ-iron phase throughout the temperature range of its existence. Likewise, the brittler low temperature allotrope of iron, α-Fe, is completely miscible with chromium above 821°C. At moderate chromium levels below 821°C, a brittle intermetallic σ-phase (β-U crystal structure) precipitates within the ferrite phase and at grain boundaries [4]; the kinetics of this process are quite sluggish. α', a finely divided embrittling intermetallic phase, can form within ferrite grains at lower temperatures. This phase, believed to be a chromium-rich product of the spinodal decomposition of ferrite [8],

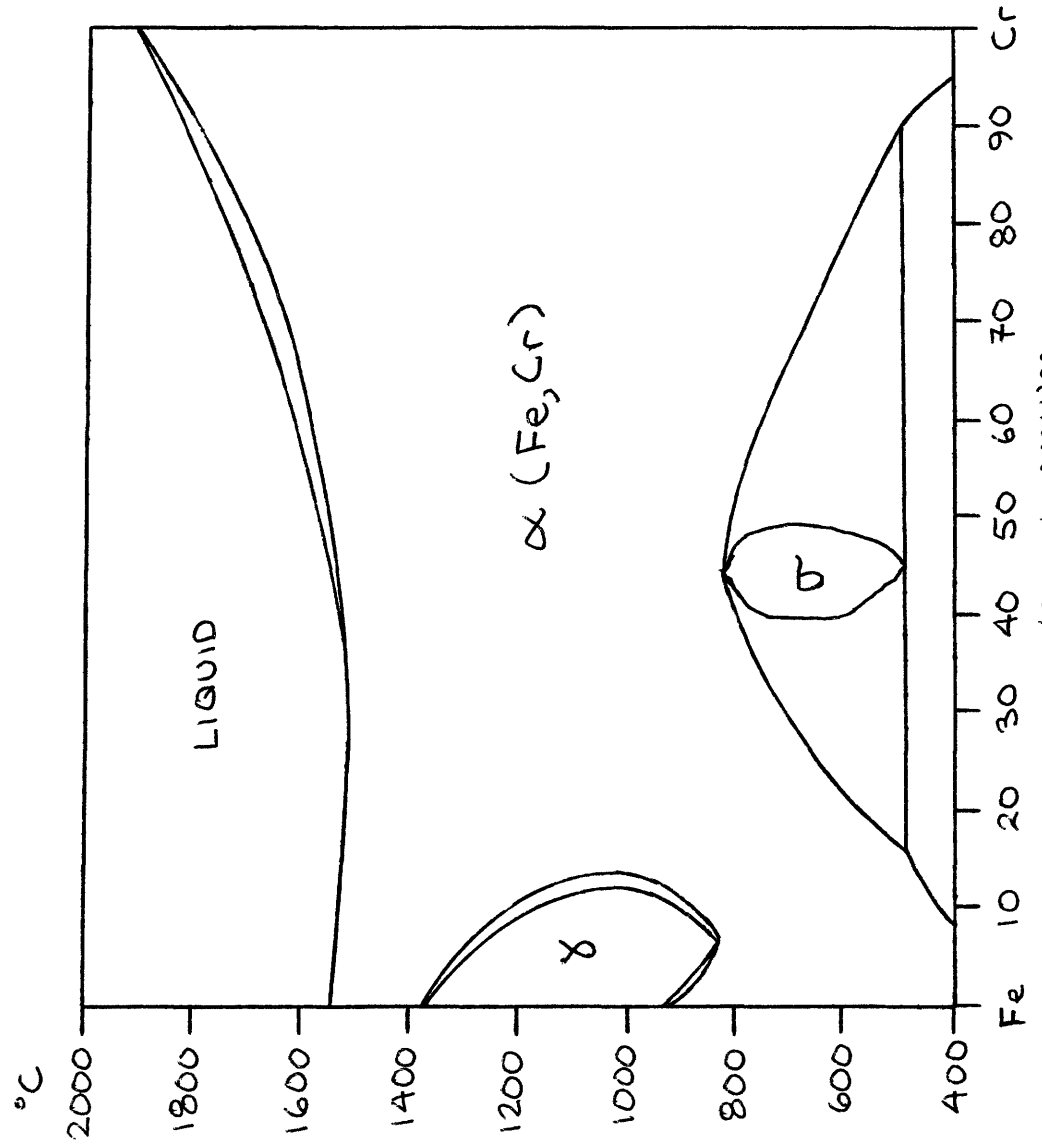

Figure 1 - Iron-Chromium Binary Phase Diagram [7]

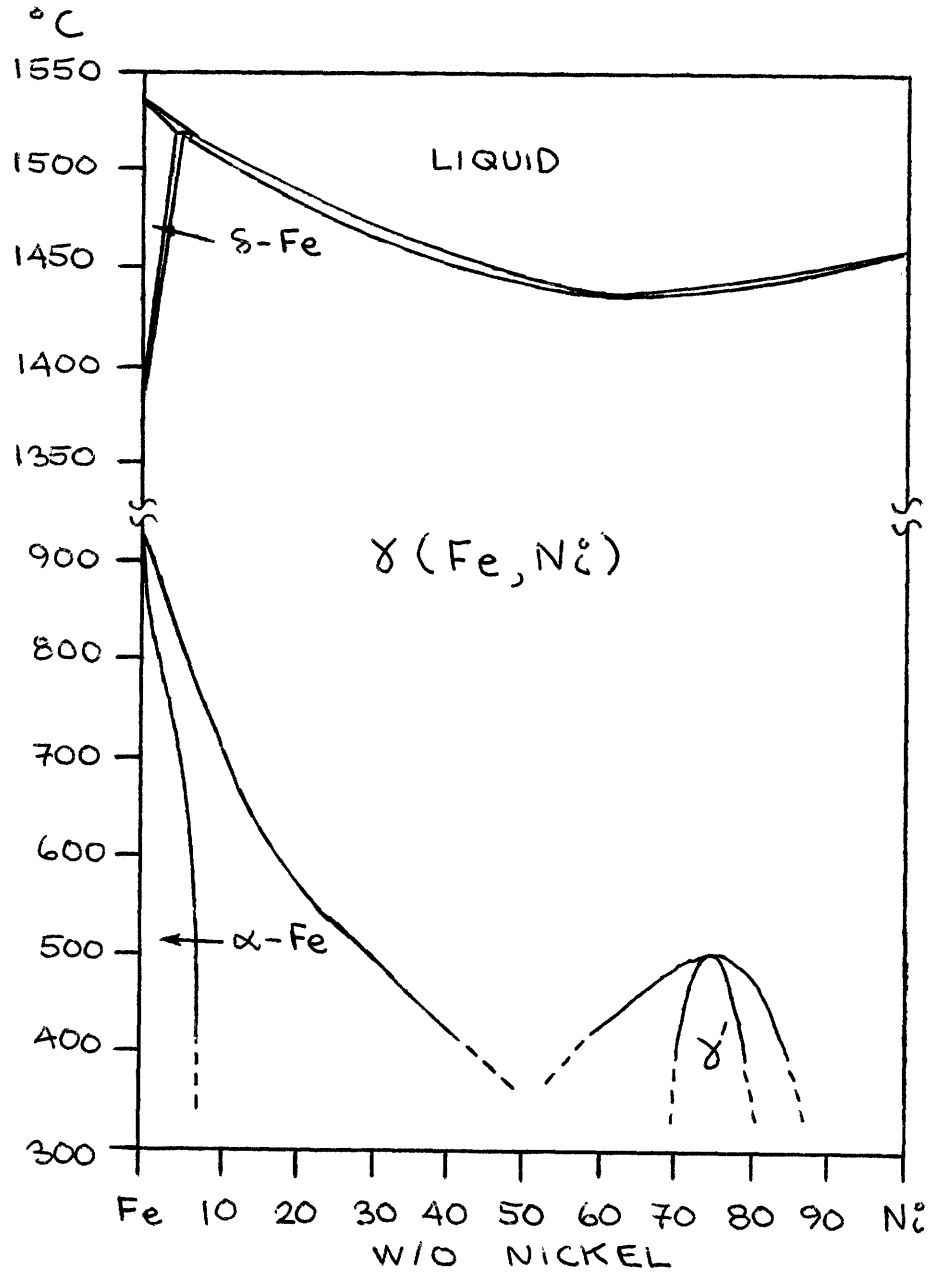

Figure 2 - Iron-Nickel Binary Phase Diagram [7]

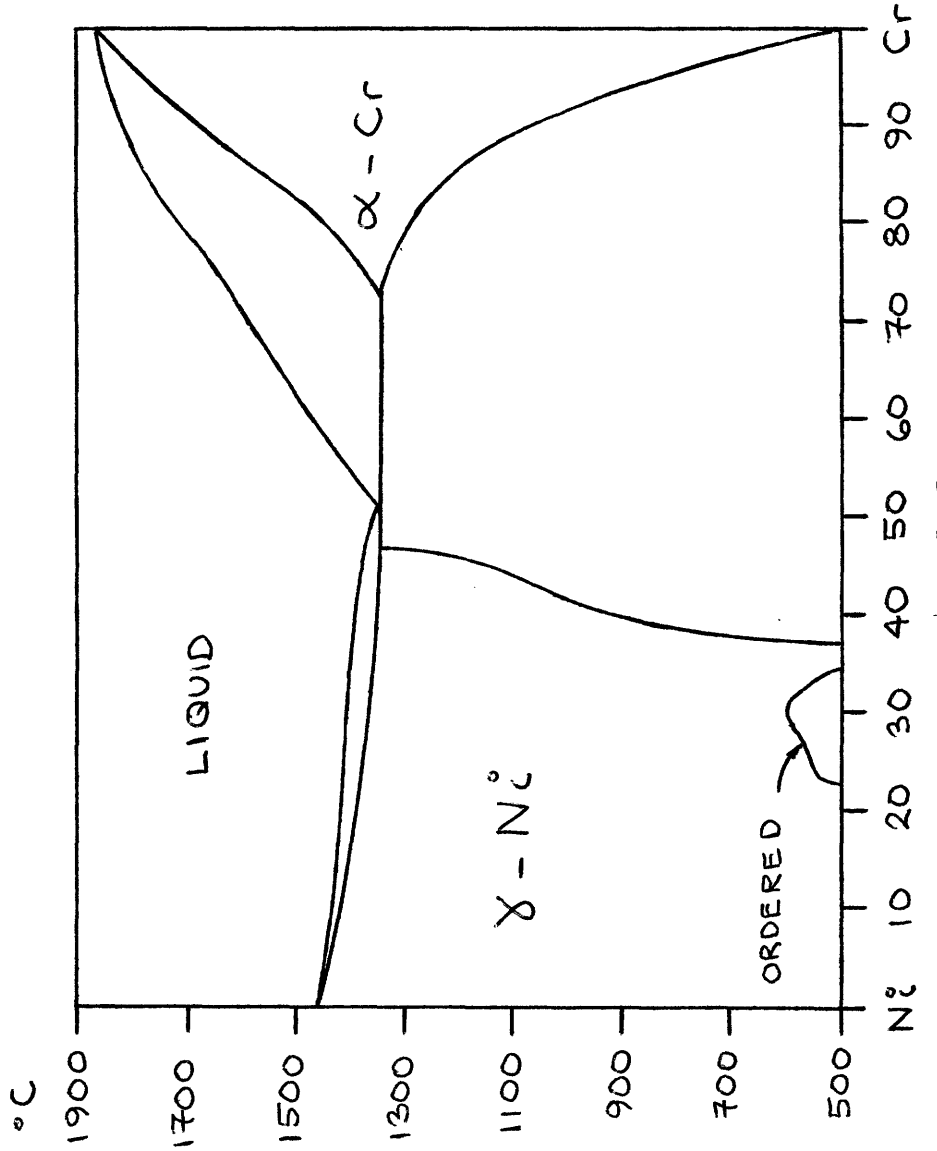

Figure 3 - Nickel-Chromium Binary Phase Diagram [7]

precipitates most rapidly in the neighborhood of 475°C and leads to the so-called "475°C embrittlement" of ferritic stainless steels. In alloys containing carbon, rapid precipitation of chromium carbide along the grain boundaries during cooling may lead to localized chromium depletion and increased susceptibility to integranular corrosion (a process known as sensitization) [9].

The recent work of Yukawa, et al. [10, 11] questions the established phase diagrams for the Cr-Ni and Cr-Fe systems. They found a δ-chromium phase with an A-15 structure at high temperatures in the chromium-rich regions of both phase diagrams. In addition, they observed a σ-phase (β-uranium crystal structure) in the Cr-Ni phase equilibrium. Though it had not been observed before, its existence is in accord with theoretical predictions [12] and extrapolation from ternary phase diagrams [13].

B. The Ternary Fe-Ni-Cr Phase Diagram

While Schafmeister and Ergang [14] show rendered sketches of the phase boundary surfaces of the Fe-Ni-Cr ternary phase diagram, the majority of the information found in the literature for this system is in the form of sections of the three-dimensional equilibrium diagram. These may be conveniently classified as vertical sections, showing the phases present as a function of the temperature and one compositional degree of freedom and horizontal (i.e. isothermal) sections, with two compositional degrees of freedom. The vertical sections may be further subdivided into radial sections, where the ratio of the weight fractions of two elements is a constant [15] and constant composition

sections, where the weight fraction of one element is unvaried [14, 16, 17]. The isothermal sections reported are either selected area diagrams, generally showing the iron-rich corner of the phase equilibrium [18, 19, 20, 21, 22] or full section diagrams [7, 10, 11, 14, 17, 23, 24, 25]. The most comprehensive modern treatment of the ternary equilibrium diagram as a whole appears in [7], and much of the discussion to follow is based on it. Typical isothermal sections, chosen to illustrate different regimes of the phase equilibrium, appear in Figures 4, 5 and 6 [7].

The liquidus and solidus surfaces of the Fe-Ni-Cr ternary phase diagram are of the sort generally seen in equilibria constrained by binary systems involving a eutectic, a peritectic and a solid solution, respectively [26]. As a result of the allotropy of iron, the austenite-stabilizing effect of FCC nickel is found to be greatest at intermediate temperatures, the ferrite-stabilizing effect of BCC chromium dominating at both higher and lower temperatures. Modest additions of nickel to the brittle intermetallic σ-phase present in the iron-chromium system (see Figure 1) are found to raise the upper temperature limit of existence of this phase to 900°C. However, the kinetics of precipitation of this Fe-Ni-Cr σ-phase are even more unfavorable than those for the σ-phase in Fe-Cr alloys. Ordered structures found in the Fe-Ni and Cr-Ni phase diagrams should appear in isothermal sections of the ternary phase diagram at low temperatures.

As somewhat of an outgrowth of the ternary phase diagram, a method

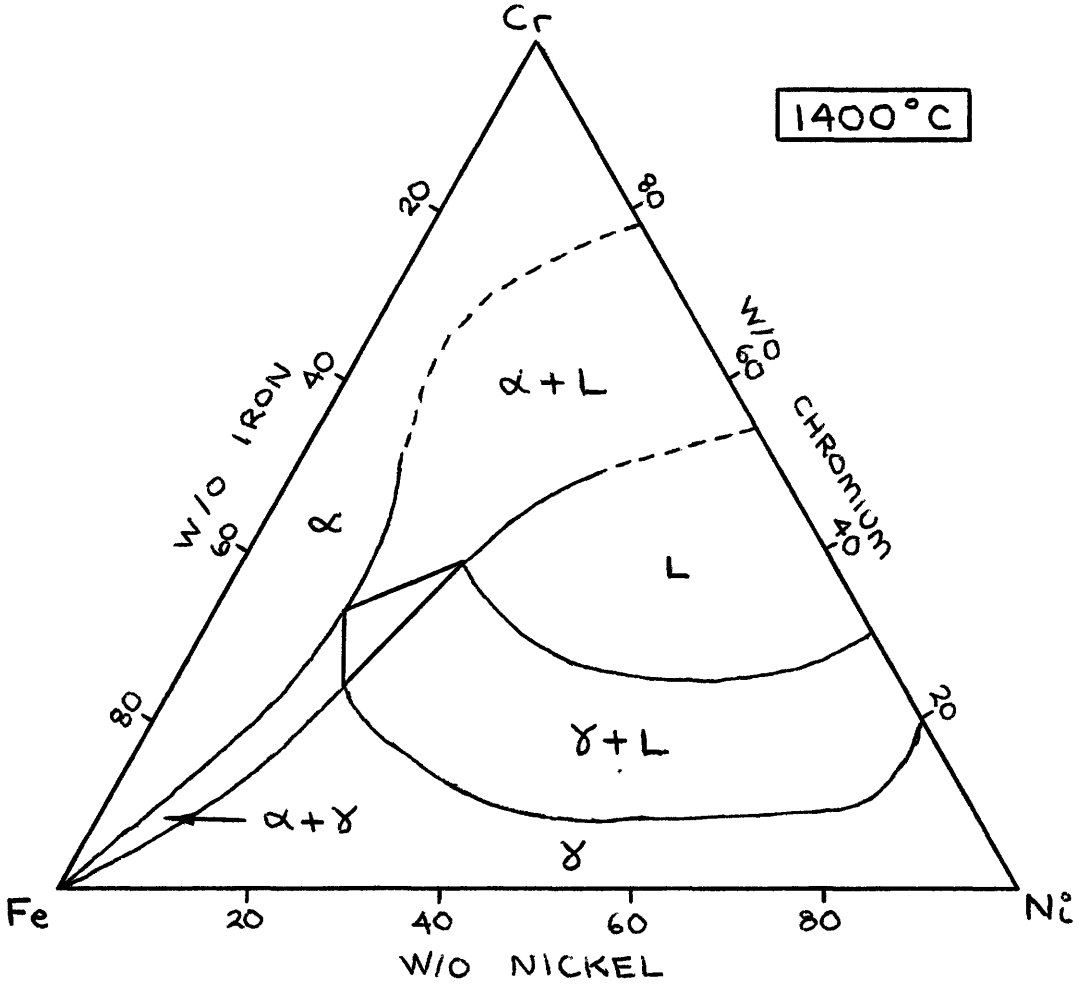

Figure 4 - 1400°C Isotherm of the Fe-Ni-Cr Ternary Phase Diagram [7]

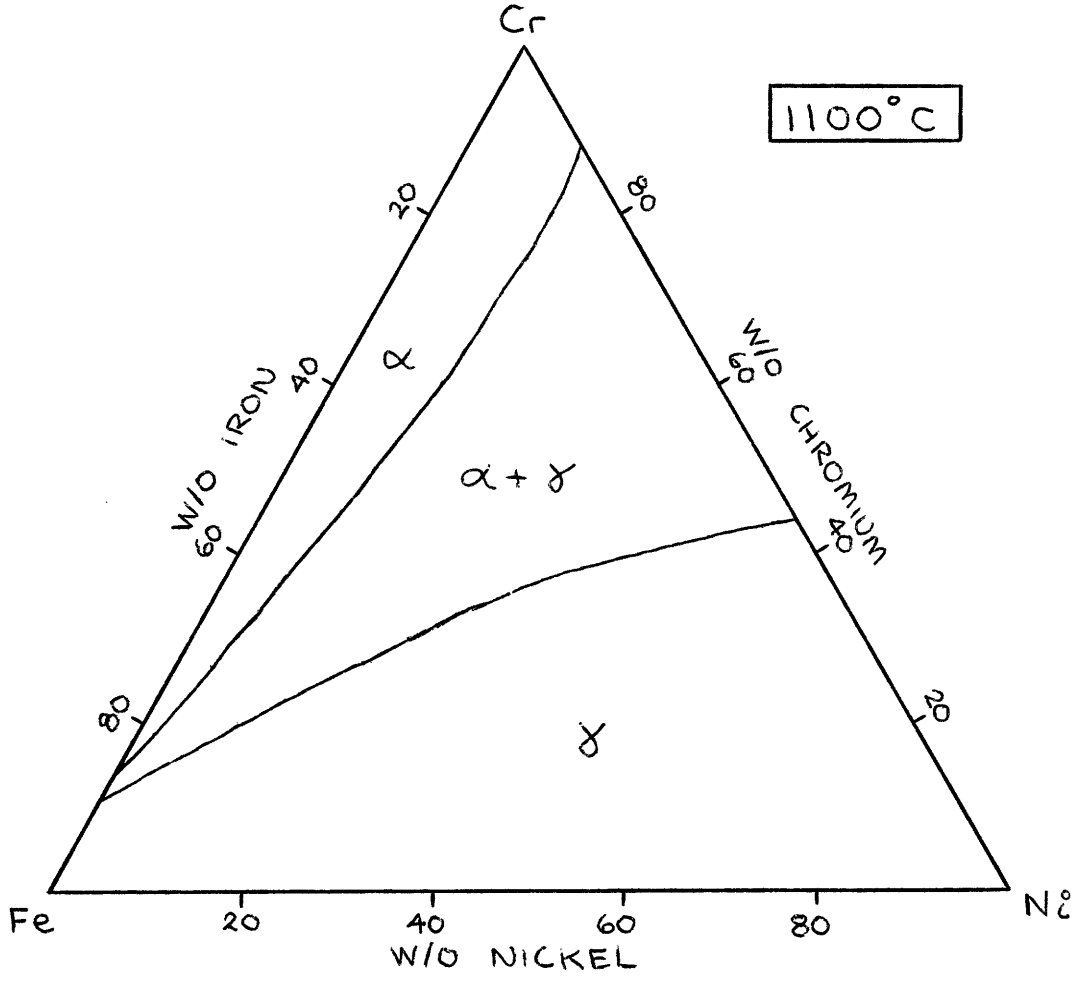

Figure 5 - 1100°C Isotherm of the Fe-Ni-Cr Ternary Phase Diagram [7]

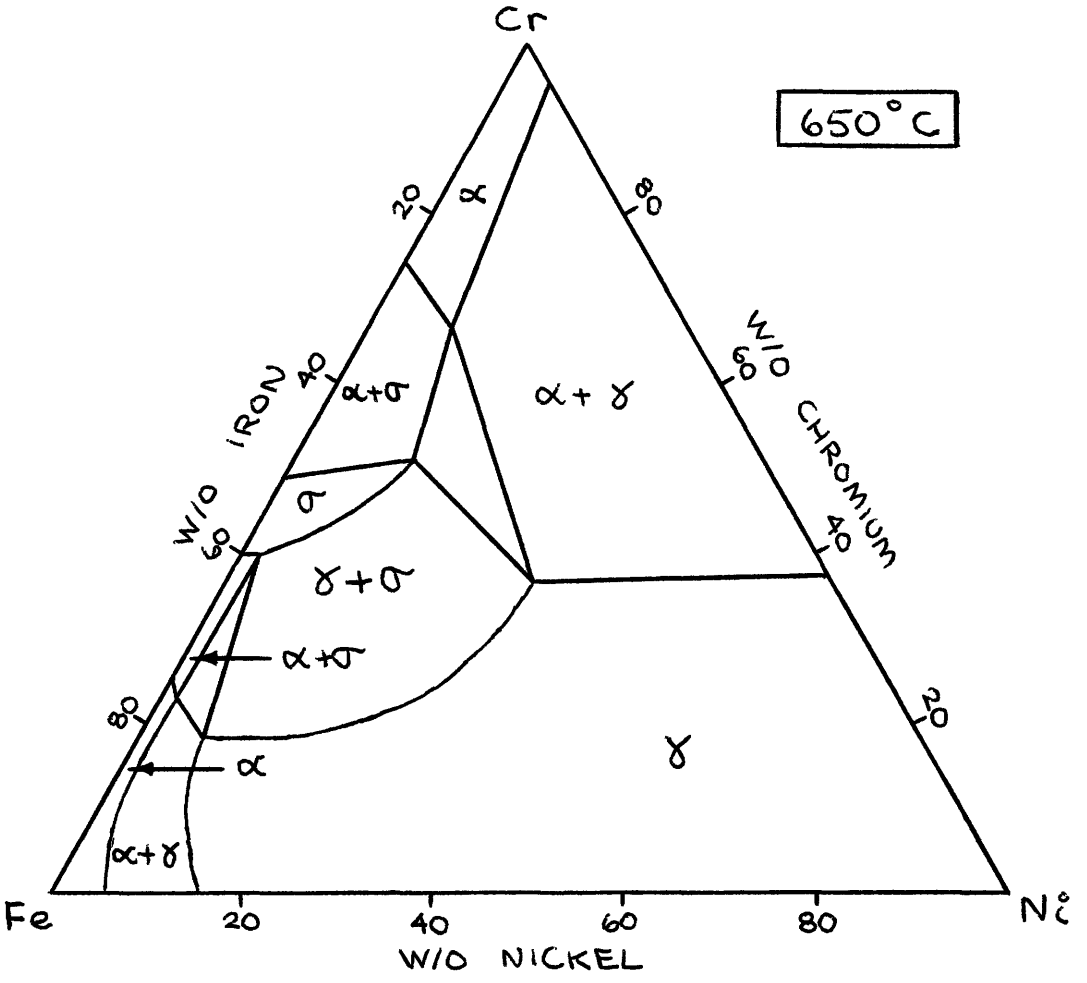

Figure 6 - 650°C Isotherm of the Fe-Ni-Cr Ternary Phase Diagram [7]

has been developed for estimating the microstructural constitution of as-deposited stainless steel weld metal from the composition of the alloy [27]. Austenite and ferrite stabilizers are grouped separately, the percentage of each element present being weighted by its relative potency in stabilizing one of the phases. Using the resulting "nickel equivalent" and "chromium equivalent" values, the expected constitution is read off Figure 7. Difficulties are encountered in the hot rolling of some austenitic stainless and heat-resistant steels when small volume fractions of ferrite are present. In order to predict the amount of ferrite in these alloys, and to aid in its control, a technique similar to that described above has been developed by Pryce and Andrews [28].

C. Tensile and Fatigue Behavior of Austenitic-Ferritic Stainless Steels

The early studies of the tensile behavior of austenitic-ferritic stainless steels were largely concerned with individual alloys; little attempt was made to consider them as a class of alloys.

The effect of cold work and various heat treatments on the mechanical behavior of an alloy containing approximately 25 w/o chromium and 4 w/o nickel were reported by Schüller and Henneke [29]. Heat treatments involving extended holding times at 650-800°C (bringing about σ-phase precipitation) or 475°C (bringing about 475°C embrittlement) were found to result in large increases in strength; little effect of other thermal histories was noted. Cold worked specimens were found to strengthen more quickly and to a larger extent than undeformed specimens.

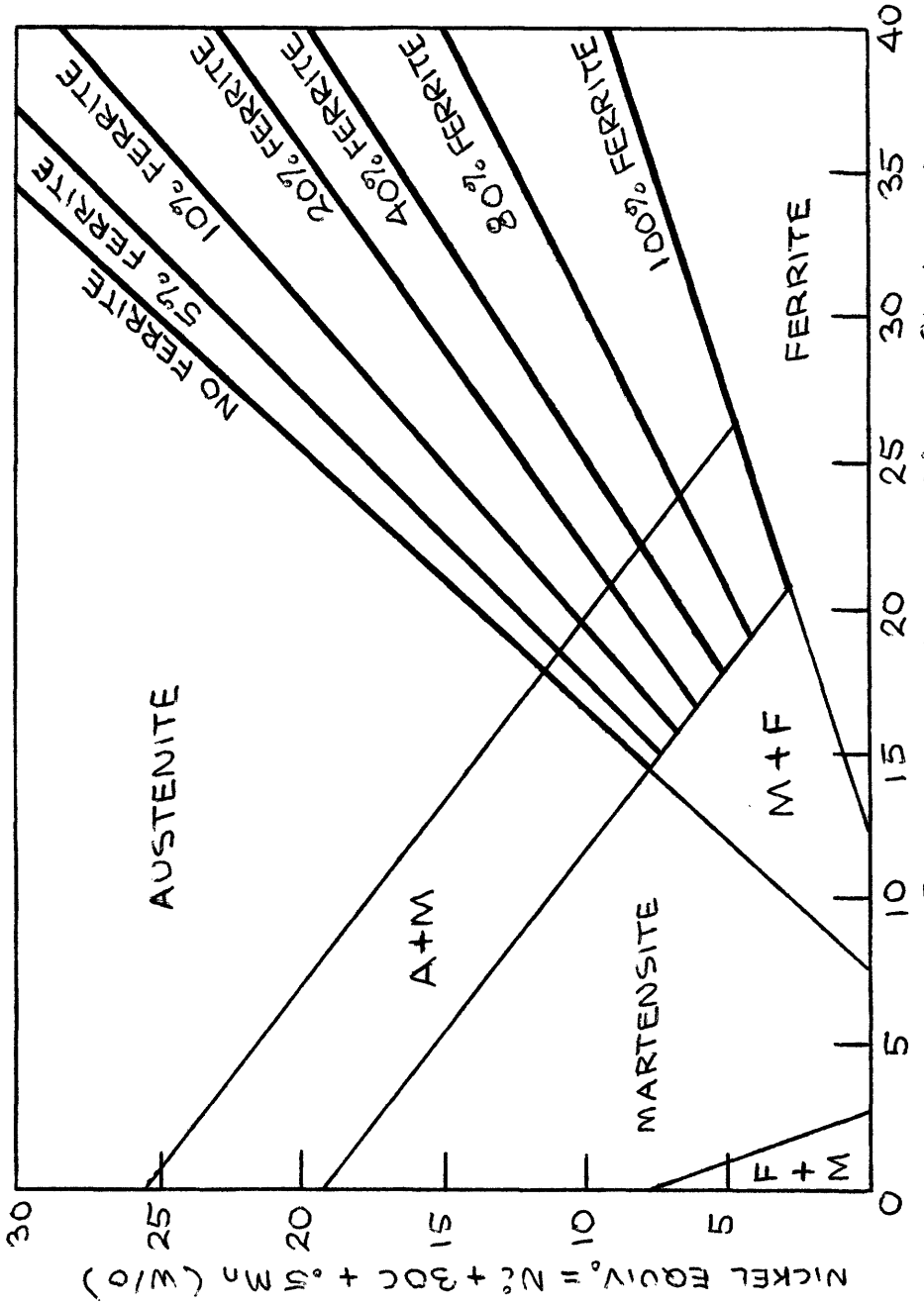

Figure 7 - Schaeffler Diagram for Stainless Steel Weld Metal [27]

The mechanical properties on IN-744, an austenitic-ferritic stainless steel containing about 26 w/o chromium and 6.5 w/o nickel were reported in two papers by workers at the International Nickel Company [20, 31]. This steel was found to combine good strength and ductility during room temperature testing (typical property values: YS=70 KSI, UTS=100 KSI, RA=30%). Work-hardening due to dislocation multiplication was found to account for the increase of flow stress with strain for small strains. Upon further deformation, transformation of the metastable austenite to martensite [32] was observed to dominate the hardening behavior. Heat treating of this steel at 475°C brought about marked embrittlement; high temperature anneals were found to bring about substantial grain size changes. As a result of its very small grain size, this alloy was found to be superplastic in the temperature range 875-975°C, undergoing elongations of at least 160% before failure.

The tensile properties of a tie-line series of austenitic-ferritic stainless steels, including alloy IN-744 described above, were first investigated by Hayden and Floreen [2]. Power Law Hardening of the ferrite phase tie-line terminus alloy was observed, with a slight upward deviation at high strains. The initially weak austenitic alloy of this series work-hardened severely as a result of the transformation of austenite to martensite. A duplex alloy was found to be weaker than either the austenitic or ferritic alloy at high plastic strains; this is presumably the result of the constraining effect of the strong ferrite phase on the shape and volume changes accompanying martensitic transformation within the austenite. While the yield strengths of the alloys were observed to

vary nearly linearly with volume fraction of ferrite for room temperature testing, their UTS values were about the same. At lower temperatures, however, the increased tendency of the austenite to form martensite when deformed was reflected in higher UTS values for the low ferrite alloys. Water quenched specimens were noted to have weaker ferrite and stronger austenite than identical specimens that had been air cooled.

The mechanical behavior of the IN-744 tie-line series alloys was also investigated by Moskovitz [1] (the steels investigated are identical to those used in this study). Moskovitz observed little dependence of the UTS on volume fraction of ferrite, while noting substantial variation in the yield strength. The yield points are in poor accord with a law-of-mixtures strength relationship. Moskovitz's tensile test results are shown in Figures 8.

The fatigue performances of several two-phase alloy systems were investigated by Hayden and Floreen [3]. They found the fatigue limits of such alloys to vary linearly with the square root of the product of their yield stress and elastic modulus. No significant effect of the duplex microstructure on the fatigue crack propagation rates or crack paths was observed. The IN-744 tie-line series steels showed a maximum fatigue limit for an alloy containing 57% ferrite. The observed dependence of the fatigue limit on the volume fraction of ferrite present is shown in Figure 9.

Moskovitz [1] investigated the corrosion fatigue and fatigue crack propagation behavior of the IN-744 tie-line series alloys. Tension-tension FCGR tests in air at R=0.05 showed the slowest crack growth rate

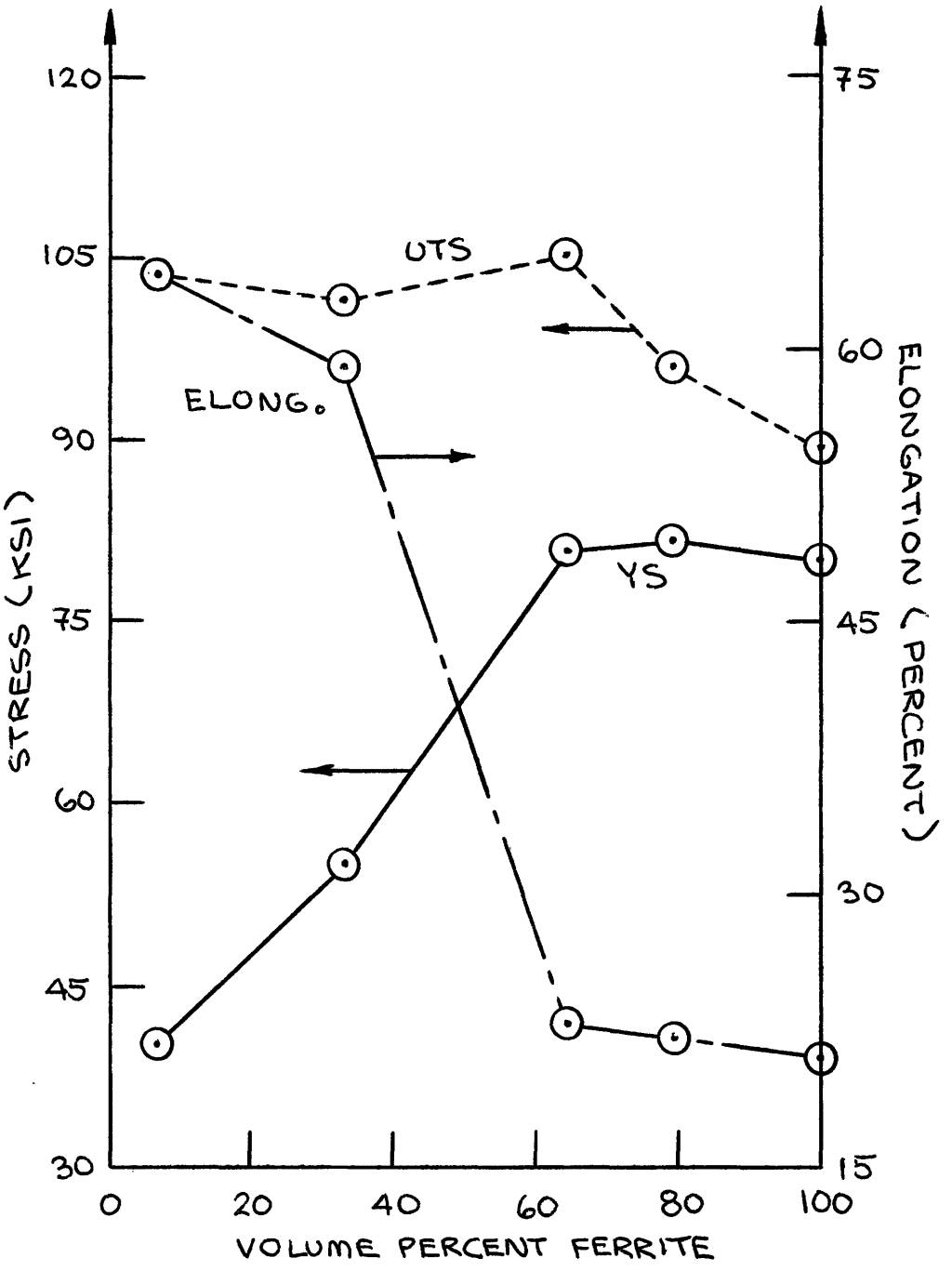

Figure 8 - Tensile Test Results for IN-744 Tie-Line Alloys [1]

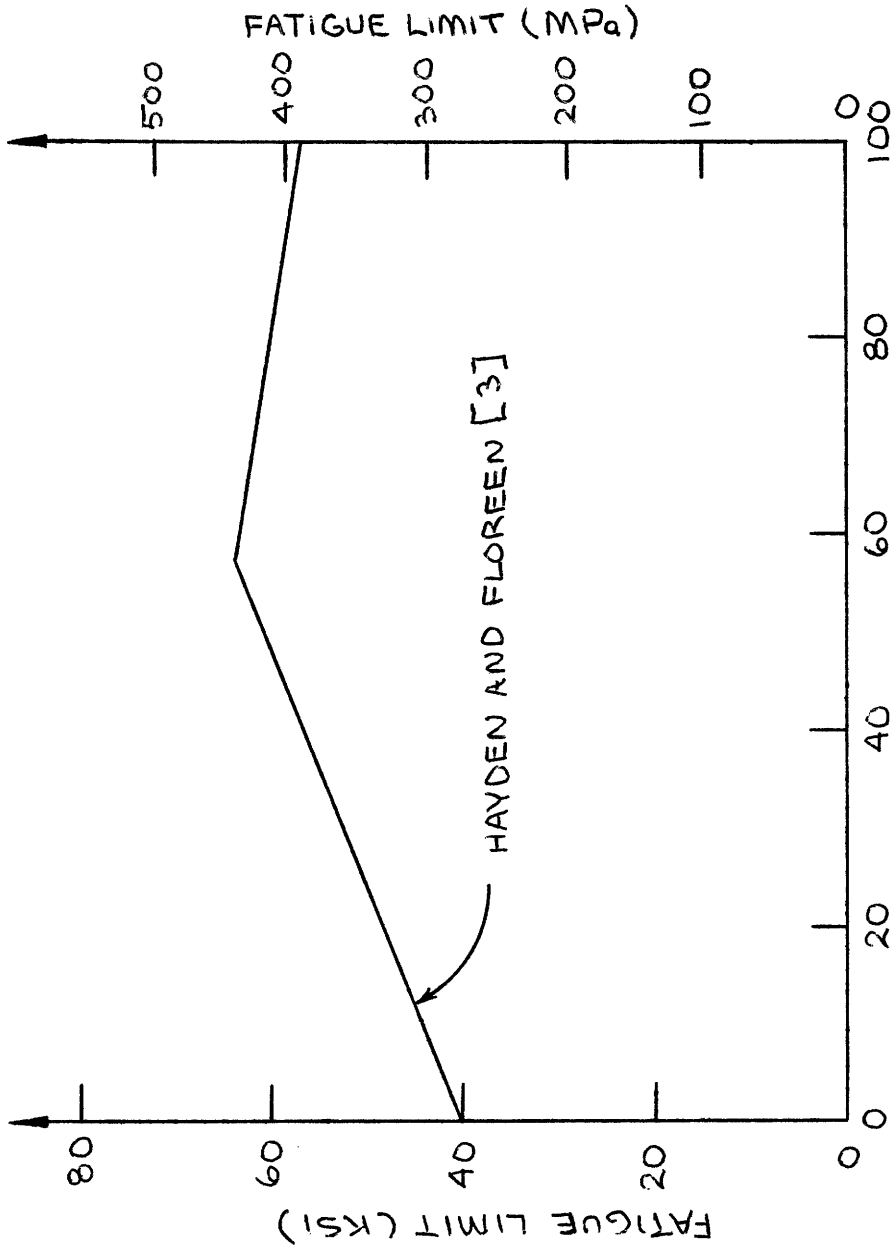

Figure 9 - Fatigue Limits of IN-744 Tie-Line Alloys [3]

to occur for the microduplex ferrite matrix alloys; at R=0.6, the ferrite matrix steels as a group showed the lowest fatigue crack propagation rates. Corrosion fatigue crack propagation tests in white water at R=0.05 showed an alloy containing 64% ferrite to perform the best. At R=0.6, however, stress corrosion cracking of the austenite phase of these alloys brought about rapid fatigue crack initiation; a purely ferritic alloy was found to have the lowest crack propagation rate.

D. Stress Corrosion Cracking of Austenitic-Ferritic Stainless Steels

Both intergranular and transgranular stress corrosion cracking have been found to occur in austenitic-ferritic stainless steels. Intermetallic or chromium carbide precipitation at phase boundaries during cooling of these alloys has been observed to cause an increased tendency to intergranular corrosive attack and stress corrosion cracking. In contrast to these findings, aging studies performed on quenched duplex stainless steels by Tedmon and Vermilyea [33] indicated that the precipitation of chromium carbide at phase boundaries may be accompanied by the transformation of some of the ferrite present to austenite. The resulting migration of the phase boundaries away from the chromium-depleted regions will minimize their effect on the stress corrosion cracking behavior of these steels. Flowers, Beck and Fontana [34] have found that ferrite additions to austenitic stainless steels generally impart improved SCC resistance. This is the result of a mechanical-electrochemical "keying effect", in which stress corrosion cracks

propagate around, rather than through, isolated ferrite aggregates. The "keying effect" has been found to be important only at lower stresses, for high stress levels tend to cause mechanical failure of the ferrite phase.

III. MATERIALS AND TEST PROCEDURES

A. Description of Alloys

Five experimental austenitic-ferritic stainless steel alloys were prepared by the General Electric Corporate Research and Development Center. The reported compositions (Table 1) lie along the IN-744 tie-line of the Fe-Ni-Cr ternary phase diagram [3]. Hence, the austenite and ferrite phase compositions in these alloys are expected to be identical.

After casting and forging, the steels were cross-rolled at 1260°C and straight-rolled to .375 - .400 in. The steels were heated to 927°C, held at temperature for 1/2 hour and rolled to .110 - .120 in. After reheating to 927°C, the experimental alloys were water quenched.

The 900°C isotherm of the Fe-Ni-Cr ternary phase diagram [25] is shown in Figure 10, and the reported compositions of the experimental alloys shown on it in Figure 11 (the minor alloying elements have been lumped with the iron for this figure).

B. Metallography

Three orthogonal sections (rolling plane, short transverse and long transverse) were cut from each alloy and mounted in bakelite as in Figure 12. The mounted samples were then ground through 600 grit silicon carbide paper and rough polished with 6μ diamond paste on a nylon wheel. Final polishing was accomplished with Syton HT-50 colloidal silica (Monsanto Corp.) on a Politex Polishing Poromeric Supreme polishing wheel (GEOS Corp.). The samples were then electroetched at 6 volts in a 10% oxalic acid solution.

Table 1 - Reported Compositions of the Experimental Alloys (weight percent)

Heat No.	C	Cr	Ni	Si	Mn
224	.02	31.8	3.2	.4	.4
225	.02	28.9	4.8	.4	.4
226	.02	25.2	5.8	.4	.4
227	.02	21.9	7.6	.4	.4
229	.02	19.5	8.8	.4	.4

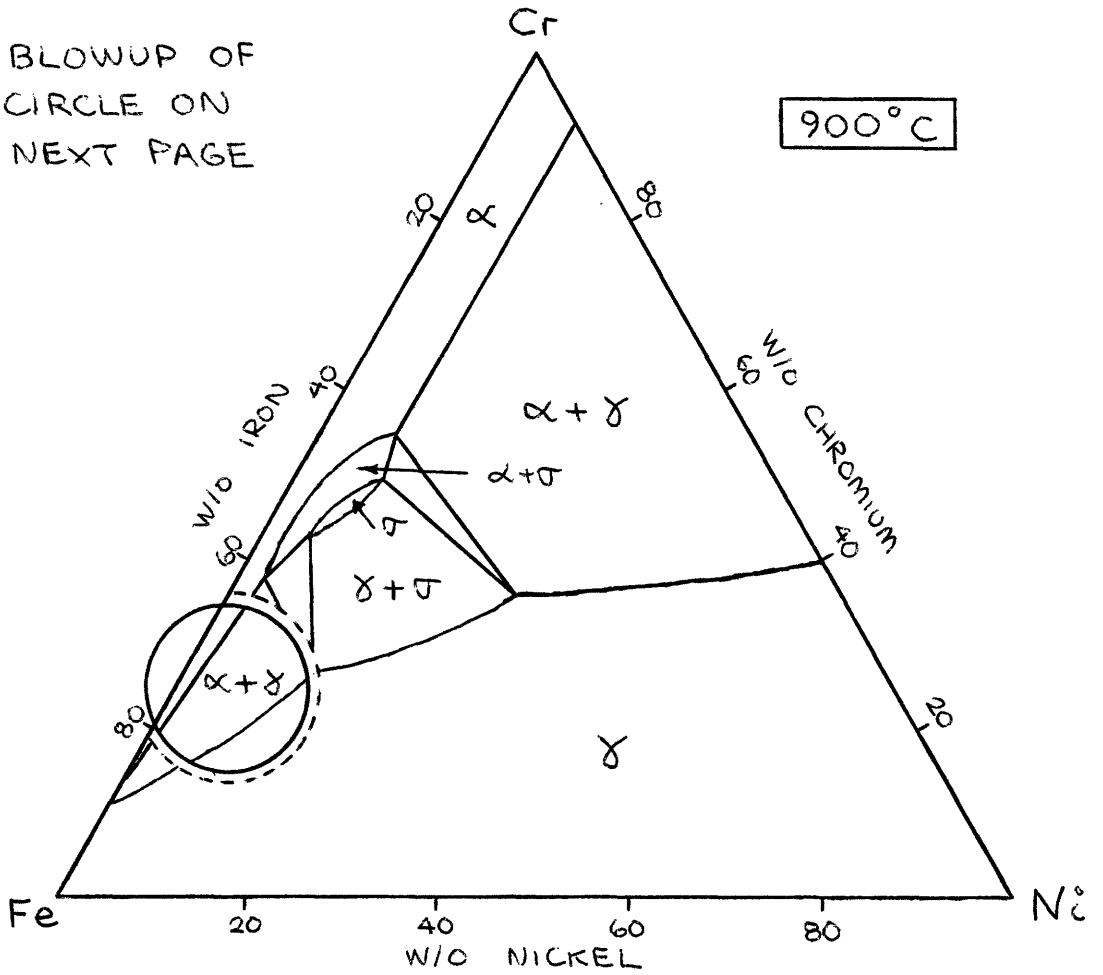

Figure 10 - 900°C Isotherm of the Fe-Ni-Cr Ternary Phase Diagram [25]

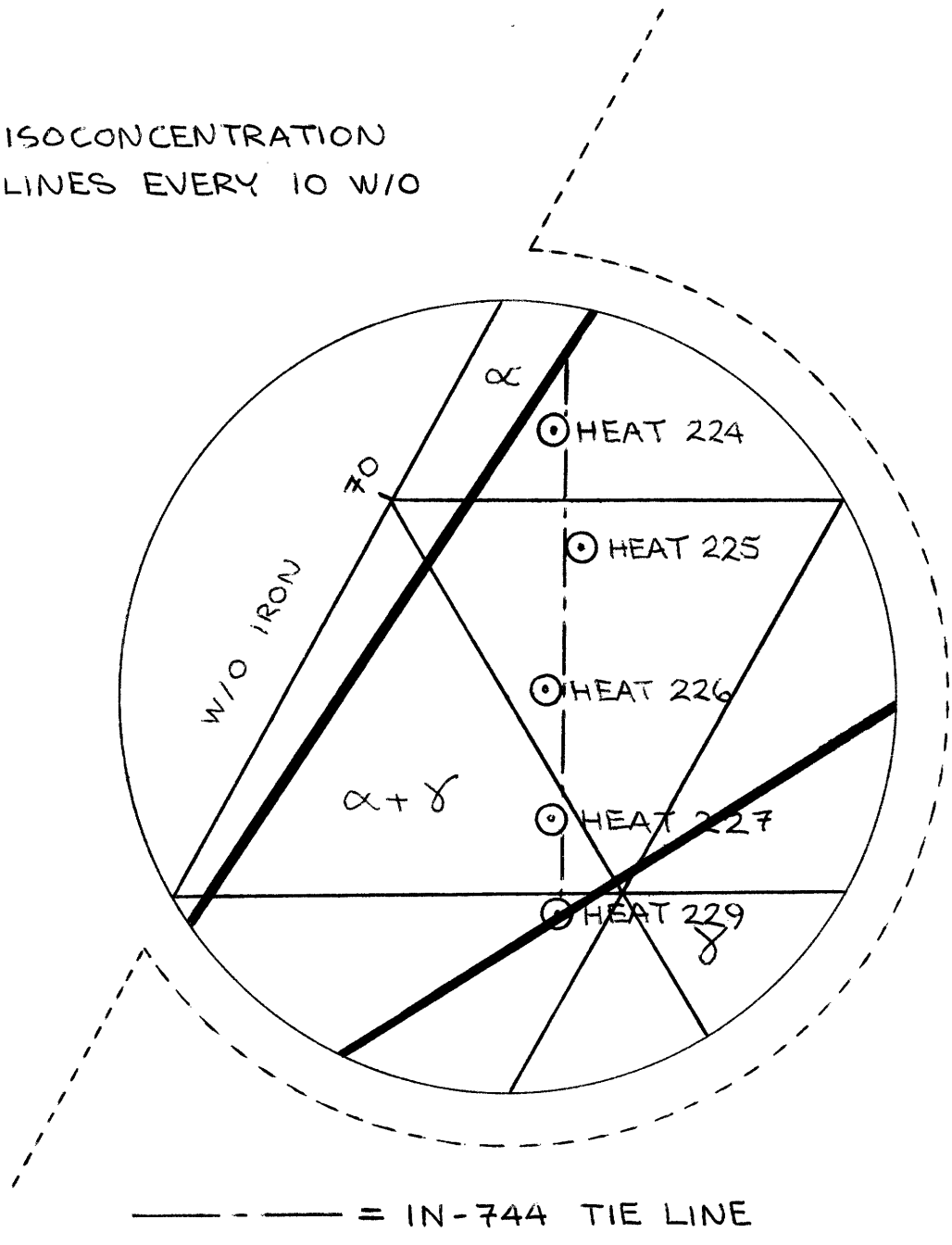

Figure 11 - Detail of Figure 10

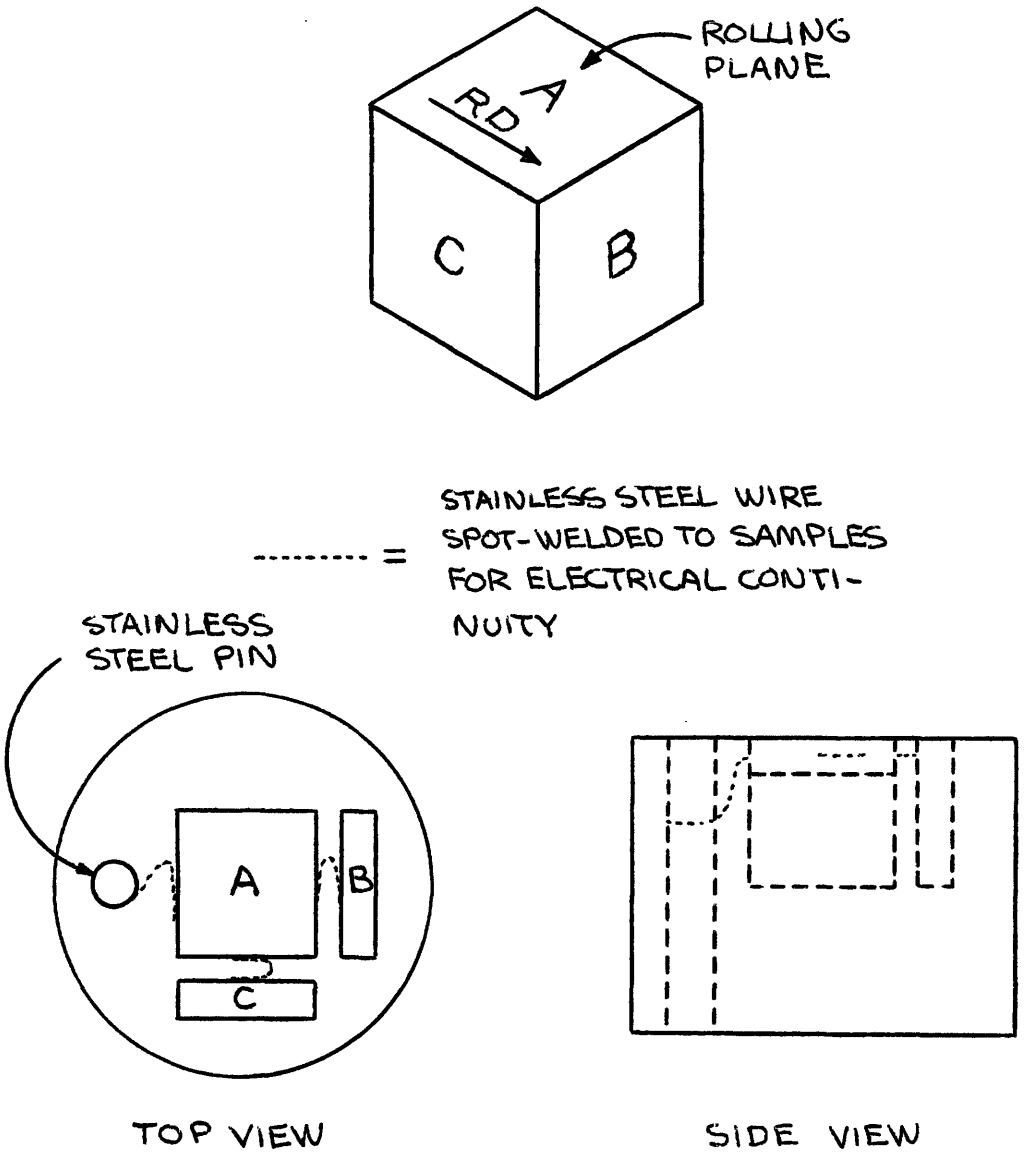

Figure 12 - Details of Metallographic Mounting of Specimens

The resulting etched surfaces were photographed at 500X, the micrographs being cut and arranged in an isometric (3-D) configuration. The volume fractions of ferrite and austenite present in the experimental alloys were determined by a random point count method [35] using 450 test points per alloy. The ferrite grain size of heat 224 was obtained by Hilliard's method [7]. The average austenite-ferrite boundary intercept distance (the reciprocal of the number of intercepts per unit length) was calculated for each alloy, and these values used to compute planar-linear orientation factors for the microstructures [36]. This factor, which assumes the value of zero for randomly oriented boundaries and has a limiting value of one, increases with both flattening of phases and their elongation in the rolling direction. As heat 224 could not be well described as planar-linear, this analysis was not performed on it.

C. Electron Microprobe Analysis

A rolling plane section of each of the five experimental alloys was mounted in bakelite in a manner similar to that shown in Figure 12. Surface preparation was largely the same as that for the metallographic specimens, but the etch was somewhat lighter to prevent excessive austenite phase surface relief and deep boundary etching.

The compositions of the steels were investigated with an automated Materials Analysis Corporation Model 5 electron microprobe. The microprobe operating conditions are shown in Table 2. The iron and nickel were analyzed with a lithium fluoride crystal, the silicon with a rubidium acid phthalate crystal, and the chromium with a pentaerythriol crystal. It was unfortunately not possible to determine the Mn content of the alloys, as

Table 2 - Electron Microprobe Operating Conditions

Accelerating Voltage	15KV
Beam size	3μ
Flag current	30na
Take-off angle	38.5°
Counting Constraints	30 seconds or 60000 counts

the Cr K_β peak interfered with the Mn K_α peak. The ferrite and austenite phases of each alloy were tested individually, at least three tests being performed on widely separated areas of each phase to ensure representative results.

D. Hardness Testing

Specimens of the experimental alloys were mechanically ground through 600 grit silicon carbide paper and their Rockwell B hardness determined on a Service Physical Testers Model 8B hardness tester. Ten tests were performed on each steel to ensure a good average hardness value and to obtain a measure of the variance of the test results.

E. S-N Testing

Ten fatigue specimens were produced from each steel (see Figure 13), hand ground through 600 grit silicon carbide paper and polished on a high speed cloth wheel with Wenol metal polish. Bending fatigue S-N tests (stress vs. number of cycles to failure) were performed on Wiedemann Baldwin Model SF-2-U bending fatigue machines in fully reversed bending at 30 CPS. Specimens not having failed by 2.5×10^6 cycles were deemed to be below their fatigue and the tests stopped. Reported stress levels are nominal maximum stresses calculated from the beam formulae:

$$\sigma_{ALT} = \frac{PLT}{2I} \quad \text{and} \quad I = \frac{WT^3}{12}$$

where: P = Alternating load amplitude

L = Specimen moment arm

T = Thickness of specimen

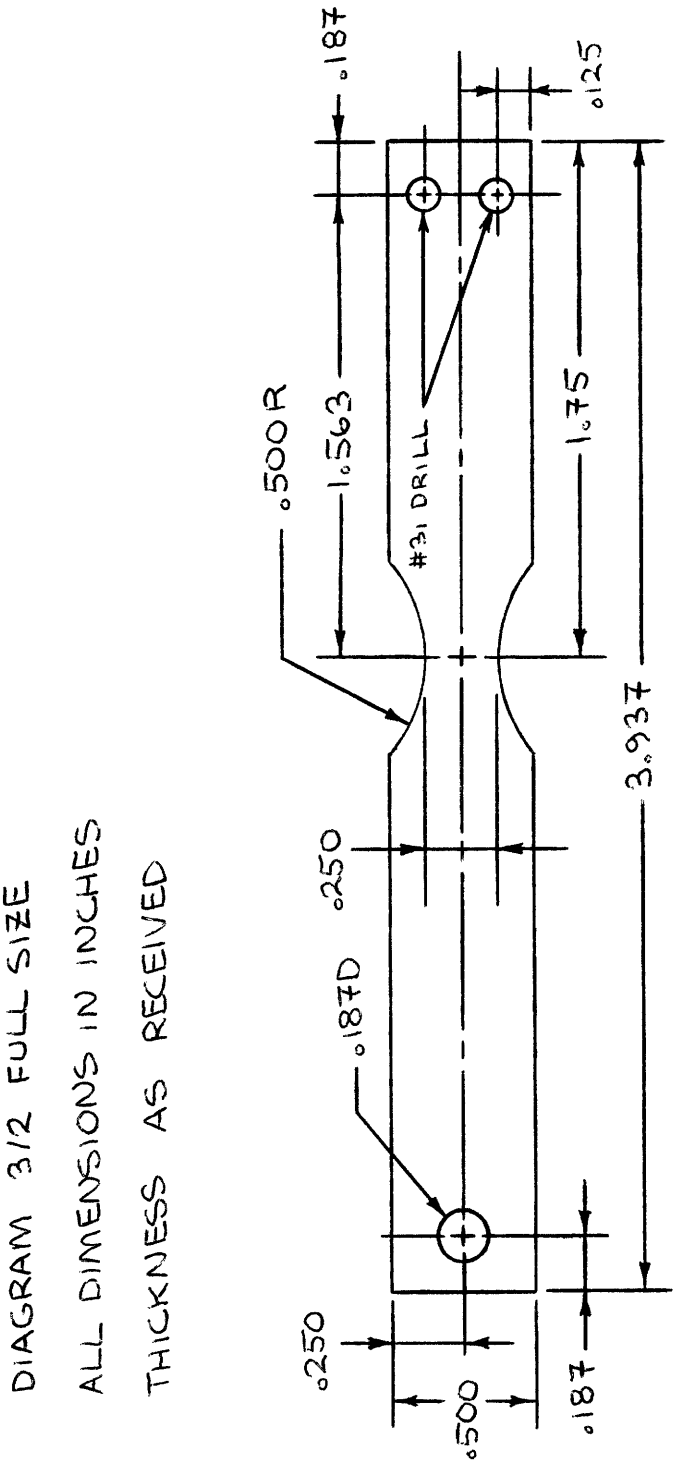

Figure 13 - Bending Fatigue Specimen Design

W = Reduced section width

The actual maximum stress amplitudes will be somewhat larger as a result of the stress concentrating effect of the reduced sections.

F. X-Ray Analysis

One inch square specimens were cut from the experimental alloys and ground through 600 grit silicon carbide paper to provide surfaces flat and acceptable for electropolishing. To remove the resulting cold-worked surface layer (∿.004 - .005 inches thick), the samples were electropolished at 10 volts in a solution composed of 64% phosphoric acid, 15% sulfuric acid and 21% water.

-325 mesh 302 stainless steel powder, with a nominal composition close to that of the austenite end of the IN-744 tie-line, was provided by the General Electric Corporate Research and Development Center. Alloy 224 (100% ferrite) was filed to produce about one gram of ferrite phase powder. The powder was sieved to -200 mesh, cleaned with acetone and vacuum annealed for 2 1/2 hours at 760°C and 2.5 X 10^{-5} torr. These powders were then sprinkled on epoxy-covered glass slides to fix them for subsequent diffractometer scans and geometrical defocussing runs.

Diffractometer scans were performed on the powder samples using chromium K_α radiation on a General Electric Model BR Type 1 diffractometer. This was both to determine the Bragg angles for the geometrical defocussing runs and to ascertain the relative integrated peak intensities to be expected for randomly oriented polycrystalline samples. The latter values were found from the scans with an integrating polar planimeter.

Diffractometer scans were also performed on the tie-line series samples, to determine the Bragg angles for pole figure runs. These scans allow a qualitative insight into the texture of the alloys, for crystallographic orientation is reflected in a difference of the relative integrated peak intensities from those calculated above. They also serve as a useful check on the pole figures, for the intensities to be expected may be calculated from the pole figures.

Pole figure runs were carried out on the powder samples using the $\{110\}_{\alpha}$ (CrK_{α}) and $\{111\}_{\gamma}$ (CrK_{α}) peaks on a Siemens type U18-003 pole figure goniometer to verify that no significant crystallographic texture was present [37]. Thereafter, the net intensities at various specimen tilt (ϕ) angleswere found by subtracting the background (off-peak) intensities from the gross intensities. The geometrical defocussing curves for the powder samples were then found by normalizing the net intensities at various ϕ angles with those at $\phi=0°$ and linearly interpolating between the calculated points.

Pole figure runs were performed on the austenite and ferrite phases of the tie-line series alloys [37]. Data for $\phi>80°$ was not used because of the large fractional noise content of the signal in this region. The trace for heat 224 proved very noisy; a laue back-reflection photograph of the surface of the specimen indicated a grain size too large for a meaningful pole figure to be constructed from a one inch square specimen. The raw data for the remaining alloys were corrected for background intensity and geometrical defocussing effects and isointensity contours

plotted on polar stereographic projection paper. These contours were then replotted on equal area projection paper and the plots integrated to determine appropriate normalization factors for absolute intensity plots. The integrations were performed by a cut and weigh procedure, each region being weighted by its average intensity. Pole figures were then produced by plotting the normalized (absolute) isointensity contours on polar stereographic projection paper.

IV. RESULTS AND DISCUSSION

A. Metallography

Isometric views of the microstructures of the experimental heats (etched to show the austenite-ferrite phase boundaries in the two-phase alloys) are shown in Figures 14-18 . Quantitative metallographic results determined from these microstructures are reported in Table 3. The expected volume fractions of ferrite in these alloys determined from the tie-line termini given by Hayden and Floreen [30] are shown for comparison. The ASTM grain size of heat 224 was found to be $3.51 \pm .2$.

The random point count ferrite volume fraction results of Moskovitz [1] deviate quite noticeably from those reported here for heats 225 and 227. The austenite phase of alloy 225 appears to have been smeared over the surface of the ferrite matrix on the surface used for Moskovitz's determination; hence, the artificially low ferrite volume fraction obtained. While no such convenient explanation exists for the deviation for heat 227, the small size of some of the austenite grains may lead to substantial human error in point counting. The point count results differ markedly from the ferrite volume fractions expected from consideration of the phase diagram. The consistently high ferrite volume fractions observed may result from incomplete transformation of ferrite to austenite during deformation and holding at 927°C.

Some interesting features of the microstructures should be carefully noted. Extensive inclusion stringering was present in alloy 224, giving rise to macroscopically observable markings on the surface of heavily

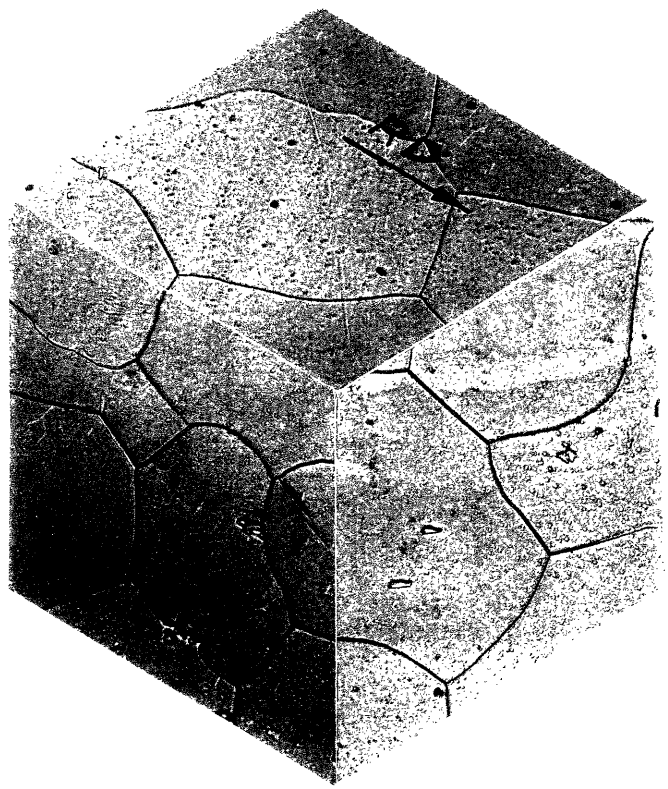

Figure 14 - Isometric View of Heat 224 Microstructure (500X)

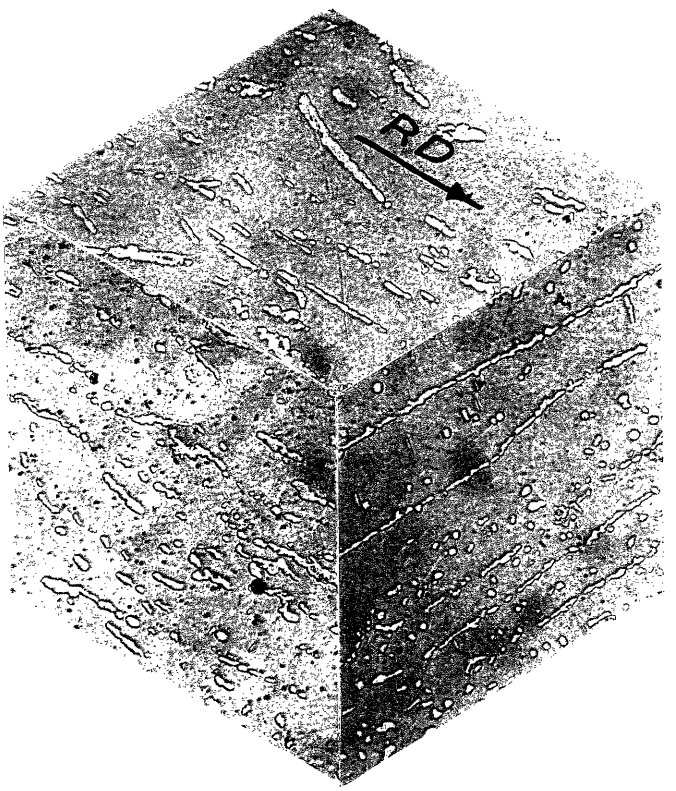

Figure 15 - Isometric View of Heat 225 Microstructure (500X)

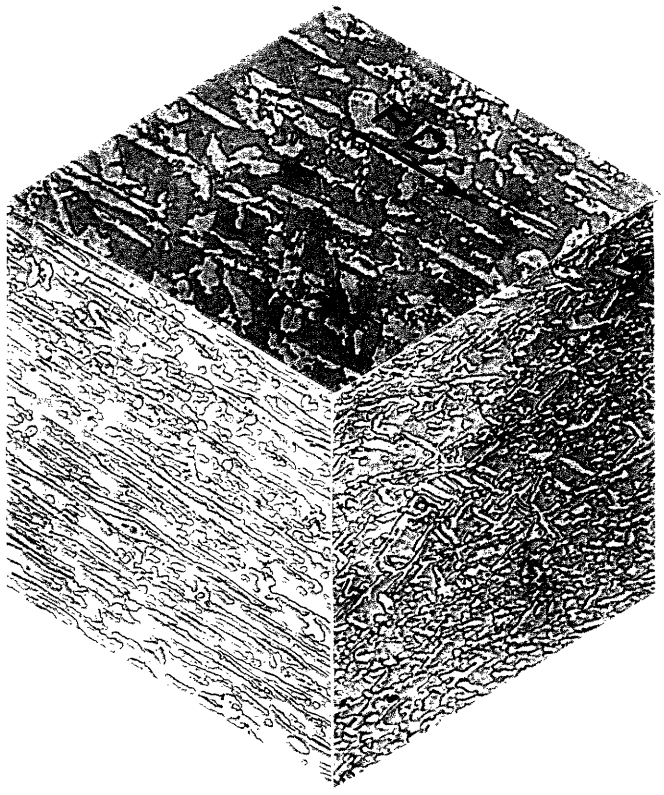

Figure 16 - Isometric View of Heat 226 Microstructure (500X)

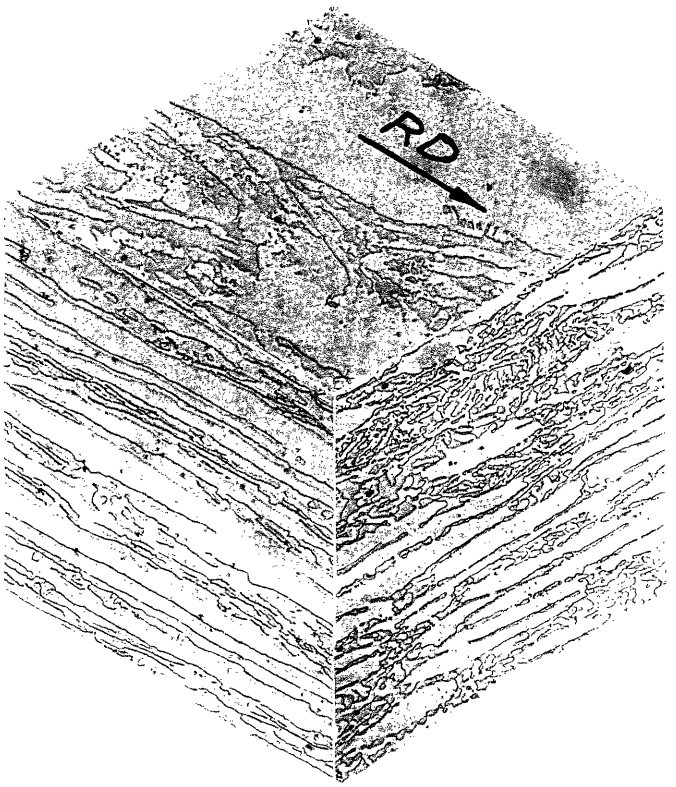

Figure 17 - Isometric View of Heat 227 Microstructure (500X)

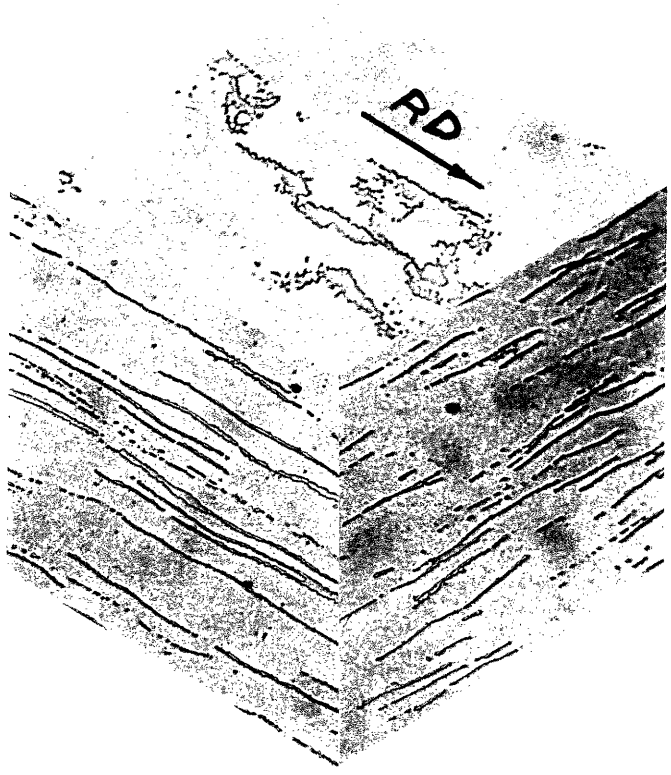

Figure 18 - Isometric View of Heat 229 Microstructure (500X)

Table 3 - Quantitative Metallography Results

Heat	Experimental v/o Ferrite	Predicted v/o Ferrite	Mean α-γ Intercept	Orientation Factor
224	100	100	∞	-
225	90.7	74.0	12.15μ	.367
226	61.4	50.1	3.43μ	.683
227	28.8	17.3	3.85μ	.713
229	7.6	0	12.90μ	.812

electropolished specimens. Heat 225 showed stringered austenite along ferrite grain boundaries oriented parallel to the rolling plane (see Figures 15 and 19). Local austenite aggregation was noted at the intersections of these stringers. The rolling plane section of alloy 226 showed a banded structure perpendicular to the rolling direction in some regions (Figure 20); this may be the result of selective recrystallization of austenite grains at coarse slip bands during hot rolling. The distribution of austenite aggregate sizes in alloy 227 (see Figure 17) is clearly bimodal. Although this steel contains 71.2% austenite, so much is present in the larger aggregates that the identity of the matrix phase in the intervening regions is a matter for debate.

Metallography of these alloys by the General Electric Corporate Research and Development Center clearly shows the austenite-austenite and ferrite-ferrite grain boundaries, giving insight into the processes which brought about the microstructures. Although substantial additions of ferrite to the austenite matrix of alloys 227 and 229 have no major effect on the austenite grain size, austenite additions appear to have a strong grain refining effect on the ferrite matrix phase of heats 224, 225 and 226. While the microstructure of heat 224 seems to be the result of unimpeded grain growth, the austenite phase seems to have successfully inhibited this process in alloy 225 (a substantial fraction of the austenite resides in the ferrite grain boundaries). In alloy 226, the ferrite grain size has been reduced to the order of the mean austenite colony spacing.

Figure 19 - Austenite Stringering in Heat 225 (500X)

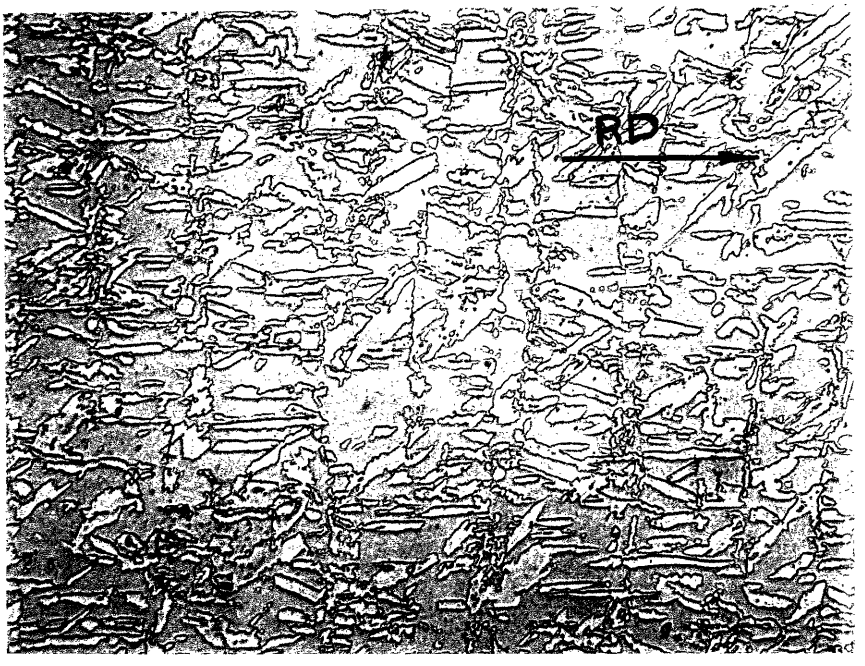

Figure 20 - Banded Structure of Heat 226 (500X)

B. Electron Microprobe Analysis

The compositions of the ferrite and austenite phases of each of the tie-line alloys as determined by the electron microprobe are shown in Table 4. It should be noted that these values do not sum to 100 w/o in all instances, even assuming some reasonable values for the manganese contents of the phases. The results are left unnormalized, as no justifiable basis for such normalization exists. The average austenite phase composition and the average ferrite phase composition of this alloy series (ignoring heat 224, as discussed below) were determined and element partition ratios (w/o in ferrite/w/o in austenite) calculated from them. These results, as well as the tie-line termini compositions of Hayden and Floreen [30], appear in Table 5.

Electron microprobe analysis of heat 224 provided unexpected results. The total of the weight percentages of the analyzed elements was consistently found to be around 90 w/o. Probe testing of iron, nickel and chromium standards indicated no calibration problems. The possibility that the reported composition of this alloy deviates significantly from its true composition cannot be easily dismissed.

Great care must be taken analyzing the microprobe results for the two-phase alloys; the results reflect the microstructure of the alloy and the geometry of the etched surface. Electron microprobe investigation of phases that are less wide than the electron beam will yield inaccurate compositional data. This will also be the case for phases that do not penetrate significantly below the plane of polish. The austenite surface relief brought about by electroetching may also be a significant source of

Table 4 - Constitution of Austenite and Ferrite Phases of Alloys (Microprobe Results)

Heat	Phase	Fe	Ni	Cr	Si
224	Ferrite	58.06	2.77	30.01	.36
225))	Ferrite	64.50	4.22	29.88	.39
225)	Austenite	67.58	8.06	23.26	.33
226))	Ferrite	66.14	3.85	28.43	.43
226)	Austenite	69.42	8.61	20.13	.34
227))	Ferrite	66.96	4.27	25.86	.35
227)	Austenite	70.31	9.09	17.87	.29
229))	Ferrite	67.54	4.12	26.66	.43
229)	Austenite	71.01	9.01	18.96	.43

Table 5 - Average Phase Compositions and Partition Ratios of Elements for the Experimental Alloys

Element	Exptl. w/o in Ferrite	Predicted w/o in Ferrite	Exptl. w/o in Austenite	Predicted w/o in Austenite	Partition Ratio
Iron	66.28	65.60	69.58	71.30	.95
Nickel	4.12	3.00	8.69	8.80	.47
Chromium	27.71	31.00	20.06	19.50	1.38
Silicon	.40	.40	.35	.40	1.15

error. The shorter X-ray path length in the ferrite phase will lead to less X-ray absorption and, as a result, enhanced count rates. The opposite will be true for the austenite phase.

Even taking the above into account, the measured compositions are in poor accord with the hypothesis that the ferrite and austenite phase compositions are constant throughout this alloy series. This may be the result of incomplete transformation of ferrite to austenite during deformation and holding at 927°C.

The partition ratios of elements between the phases of the tie-line alloys are in good agreement with thermodynamic predictions. FCC nickel, a strong austenite stabilizer,is 2.11 times as prevalent in the austenite phase as in the ferrite phase. Likewise, the ferrite phase contains 1.38 times as much chromium, a BCC α-iron stabilizer, as the austenite phase.

C. Hardness Testing

The average hardness values for the tie-line series alloys are shown in Table 6; they are plotted with the yield point data of Moskovitz [1] in Figure 21 .

In view of the functional relationship between the flow curve of a material and its hardness [38], the correlation between the hardness and yield point values of Figure 21 is not surprising. Since some of the steels of this series are strongly work-hardening, it is best not to assert a direct relationship between yield strength and hardness for them.

The shallow upward slope of the hardness and yield point values for the ferrite matrix alloys with increasing austenite additions may be easily

Table 6 - Hardness Test Results

Heat	R_B Hardness	σ_{R_B}
224	90.5	1.43
225	91.8	1.69
226	93.8	.92
227	86.8	2.62
229	81.0	1.55

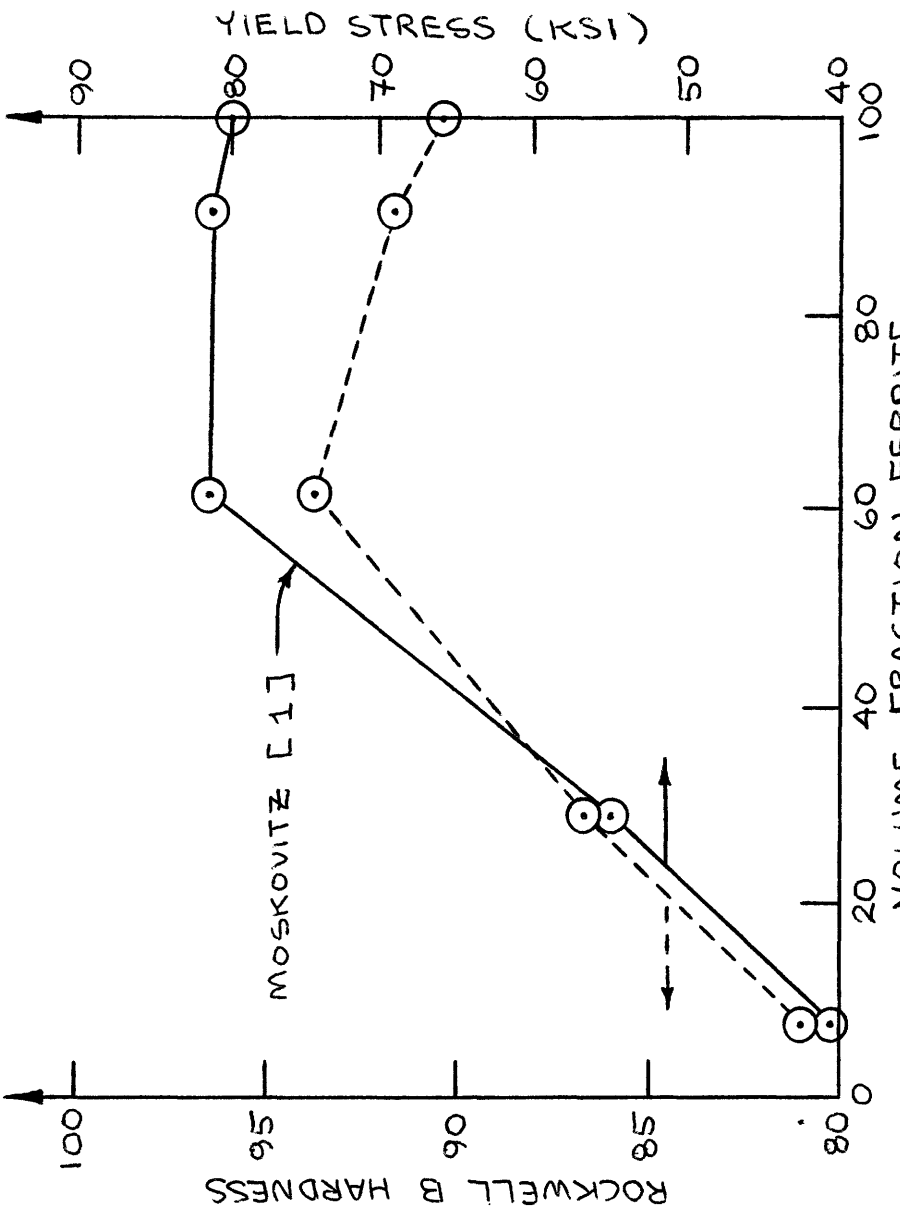

Figure 21 - Dependence of Rockwell B Hardness and Yield Stress [1] of Experimental Alloys on Volume Fraction of Ferrite

rationalized. The yield point decrease resulting from the law-of-mixtures strength of the duplex structure (the austenite is substantially weaker than the ferrite) will be outweighed by the strength increase resulting from the strong grain refining effect of the increasing austenite additions on the ferrite matrix. The austenite matrix alloys (heats 227 and 229) show no significant dependence of austenite grain size on ferrite volume fraction; thus, the sharp increase in hardness and yield strength with ferrite additions may best be explained by a law-of-mixtures strengthening of the weaker austenite matrix by the ferrite phase.

D. S-N Testing

The S-N curves for the experimental alloys are shown on a log-linear plot in Figure 22. Linear least-squares data fits to the equation log (life) = $A\sigma + B$ for samples that failed resulted in the downward-sloping portions of these curves. The slope and intercept values (A and B) for each alloy are reported in Table 7. As the number of tests was insufficient to accurately determine the fatigue limits for these alloys, the values chosen were the tested stress levels below which all properly prepared samples ran to 2.5×10^6 cycles without failure. These fatigue limits, as well as those determined by Hayden and Floreen [2], are plotted against volume percent ferrite in Figure 23 (see Table 8).

The effect of the volume fraction of ferrite present on the fatigue crack initiation life-times of the experimental alloys probably involves contributions from two sources. The variation of yield stress with ferrite volume fraction (discussed in the previous section) will certainly

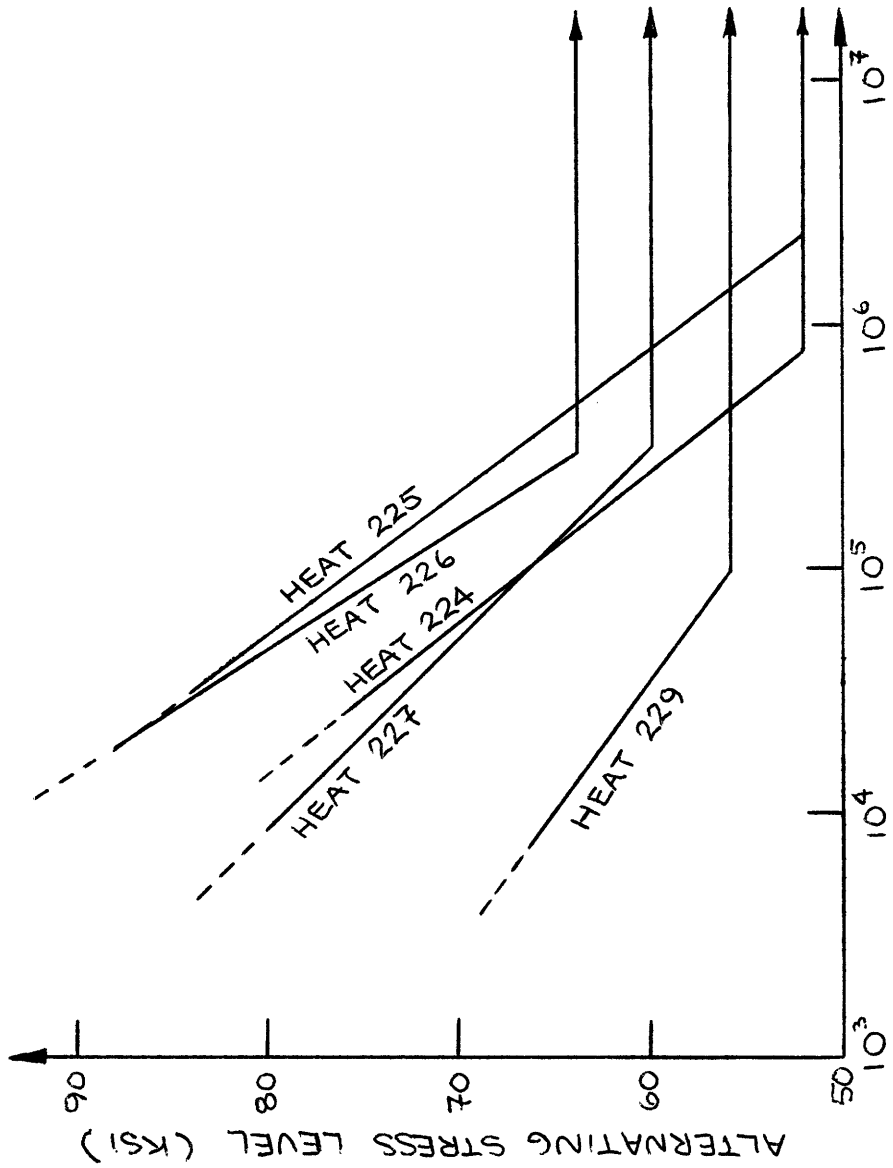

Figure 22 - S-N Test Results for Experimental Alloys

Table 7 - Slope-Intercept Data for Linear Portions of S-N Curves (Log(Life) = $A\sigma+B$)

Heat	$A(KSI^{-1})$	B
224	-.06172	9.1067
225	-.05826	9.3889
226	-.04925	8.6346
227	-.07653	10.081
229	-.11107	11.198

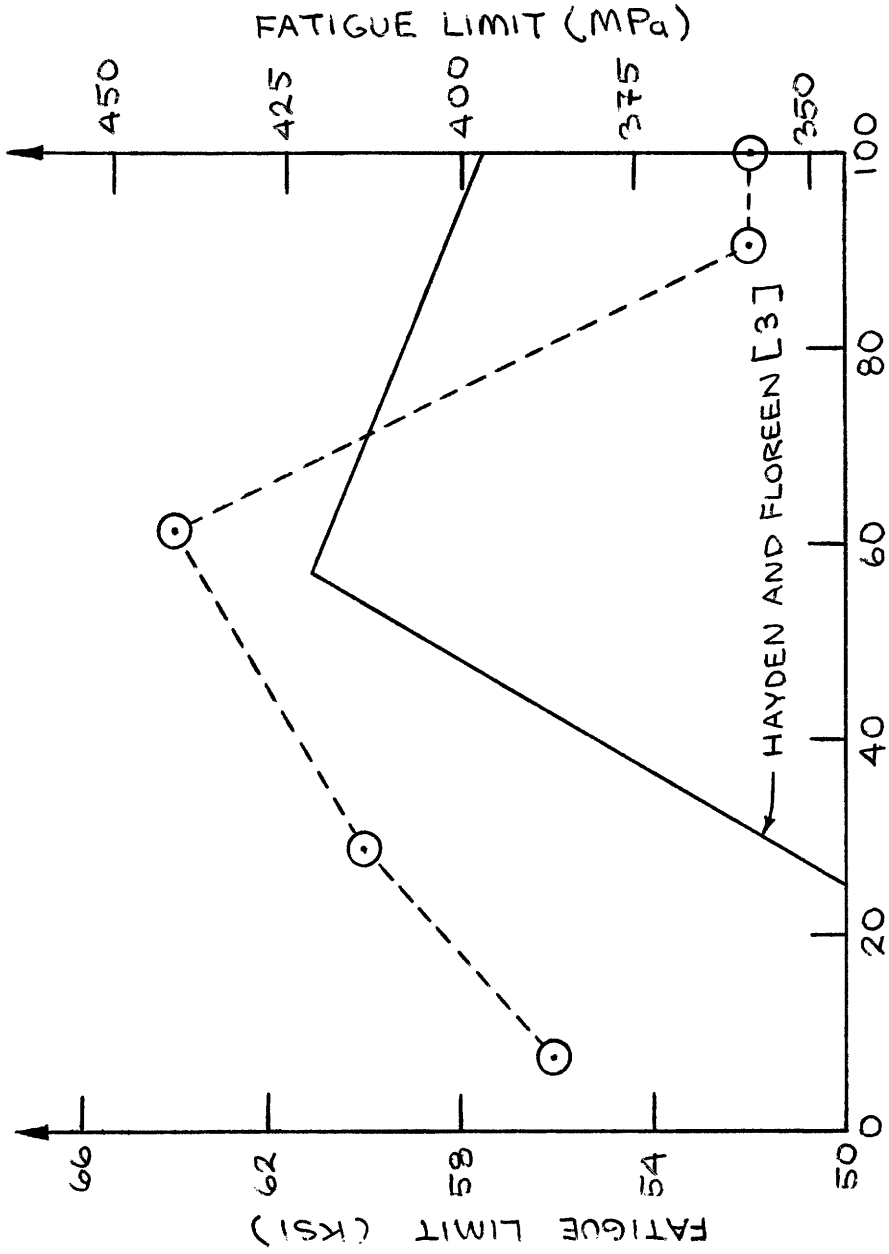

Figure 23 - Dependence of Fatigue Limit of IN-744 Tie-Line Alloys (this Study and [3]) on Volume Fraction of Ferrite

Table 8 - Fatigue Limits of Experimental Alloys

Heat	Fatigue Limit (KSI)
224	52
225	52
226	64
227	60
229	56

play an important role. The strength increments resulting from increasing additions of the minority phase in these alloys seems to be reflected in their initiation lifetimes. The ability of the fine scale duplex microstructures of heats 225, 226 and 227 to disperse slip and delay crack initiation seems to enhance initiation resistance even further. The duplex microstructures will also tend to slow crack propagation by mitigating against low energy fracture modes in the ferrite phase.

The disparity between the fatigue limits reported here and those of Hayden and Floreen [3] may be easily explained. The air-cooled specimens used in their investigation will have a harder ferrite phase and a softer austenite phase than the water-quenched specimens used in this study. Thus, a lower fatigue limit will be expected for their low-ferrite alloys, and a higher fatigue limit for their high-ferrite alloys [2]. Also, since their specimens ran forty times as long as those of this investigation, their fatigue limit results are expected to be noticeably lower in general.

Testing of broken fatigue specimens of alloy 229 with a magnet indicated the presence of a significant amount of strain-induced martensite in the vicinity of the crack. This was not found to be as noticeable an effect in the other alloys, where the fine scale duplex microstructure acts to limit the ability of the ferrite phase to accommodate the shape and volume change accompanying the transformation.

Scanning electron fractography of the broken fatigue crack growth rate specimens of Moskovitz [1] showed relatively featureless surfaces.

This is in good accord with the observations of Hayden and Floreen [3] and indicates that the fatigue crack paths are not drastically influenced by the alloy microstructures.

E. X-Ray Analysis

The relative integrated peak intensities of the single phase powder samples and of the ferrite and austenite phases of the experimental alloys are reported in Tables 9, 10 and 11. Normalized net intensities for the austenite and ferrite powder samples at selected tilt (ϕ) angles are shown in Table 12, and the resulting geometrical defocussing curves plotted in Figures 24 and 25. Pole figures for the ferrite and austenite phases of the experimental alloys are shown in Figures 26 - 33.

Comparison of the relative integrated peak intensities of the experimental alloys with those of the powder samples clearly indicates the presence of crystallographic texture in all phases of the alloy series. Thus, the sharp intensity maxima on many of the pole figures are not surprising. The match between the locations of the intensity maxima for the ferrite and austenite pole figures of each of alloys 225, 226 and 227 is startingly good. This shows that the Kurdjumov-Sachs relationship, $\{110\}_\alpha\ [111]_\alpha \parallel \{111\}_\gamma\ [110]_\gamma$ [39], which minimizes the phase boundary energy in austenitic-ferritic alloys, plays a large role in the development of hot rolling textures in these materials. The absence of a strong maximum in the austenite phase pole figure of alloy 229 is probably a result of the small fraction of the total austenite grain boundary area made up by phase boundaries. The geometric constraints

Table 9 - Relative Integrated Peak Intensities for Powder Samples

Powder	Peak	Relative Integrated Peak Intensity
Ferrite	$\{110\}_{\alpha}(K_{\alpha})$	(100)
Ferrite	$\{200\}_{\alpha}(K_{\alpha})$	39.08
Austenite	$\{111\}_{\alpha}(K_{\alpha})$	(100)
Austenite	$\{200\}_{\alpha}(K_{\alpha})$	67.66
Austenite	$\{220\}_{\alpha}(K_{\alpha})$	116.88

Table 10 - Relative Ingegrated Peak Intensities for Ferrite Peaks of Experimental Alloys

Heat	Peak	Relative Integrated Peak Intensity
224	$\{110\}_{\alpha}(K_{\alpha})$	(100)
224	$\{200\}_{\alpha}(K_{\alpha})$	3.30
225	$\{110\}_{\alpha}(K_{\alpha})$	(100)
225	$\{200\}_{\alpha}(K_{\alpha})$	1.58
226	$\{110\}_{\alpha}(K_{\alpha})$	(100)
226	$\{200\}_{\alpha}(K_{\alpha})$	6.87
227	$\{110\}_{\alpha}(K_{\alpha})$	(100)
227	$\{200\}_{\alpha}(K_{\alpha})$	50.46
229	$\{110\}_{\alpha}(K_{\alpha})$	(100)
229	$\{200\}_{\alpha}(K_{\alpha})$	16.22

Table 11 - Relative Integrated Peak Intensities for Austenite Peaks of Experimental Alloys

Heat	Peak	Relative Integrated Peak Intensity
225	$\{111\}_\gamma (K_\alpha)$	(100)
225	$\{200\}_\gamma (K_\alpha)$	22.86
225	$\{220\}_\gamma (K_\alpha)$	2.86
226	$\{111\}_\gamma (K_\alpha)$	(100)
226	$\{200\}_\gamma (K_\alpha)$	73.19
226	$\{220\}_\gamma (K_\alpha)$	39.36
227	$\{111\}_\gamma (K_\alpha)$	(100)
227	$\{200\}_\gamma (K_\alpha)$	454.54
227	$\{220\}_\gamma (K_\alpha)$	12.47
229	$\{111\}_\gamma (K_\alpha)$	(100)
229	$\{200\}_\gamma (K_\alpha)$	54.55
229	$\{220\}_\gamma (K_\alpha)$	42.89

Table 12 - Geometrical Defocussing Curve Data

Tilt Angle	Net Intensity Ratio	
	Austenite	Ferrite
0°	1.000	1.000
10°	1.000	1.000
20°	1.000	1.000
30°	.964	.955
40°	.931	.910
50°	.842	.838
60°	.707	.725
70°	.495	.528
75°	.361	.394
80°	.205	.242
85°	.073	.055
90°	0	0

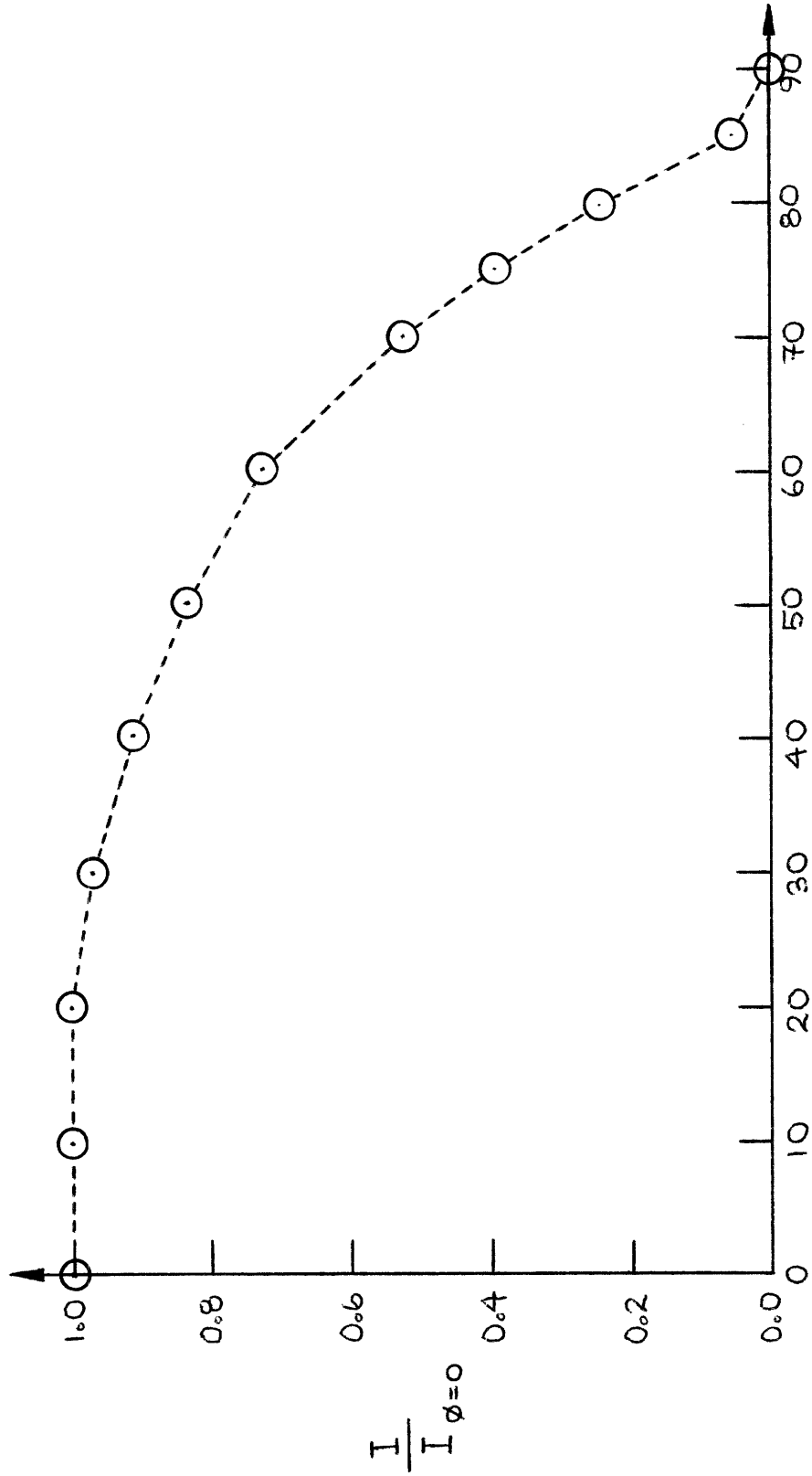

Figure 24 - Ferrite Phase Geometrical Defocussing Curve ({110} Peak)

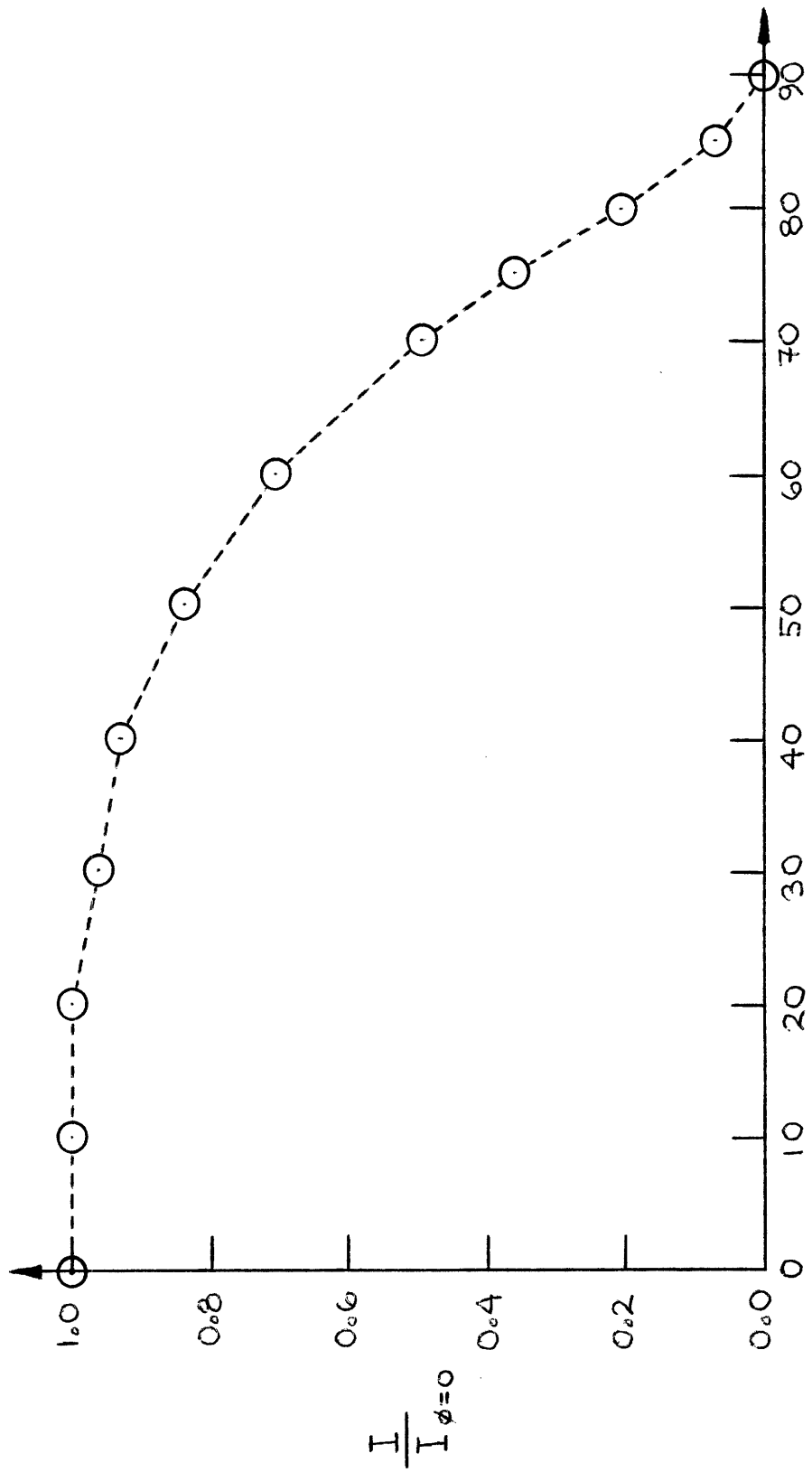

Figure 25 - Austenite Phase Geometrical Defocussing Curve ({111} Peak)

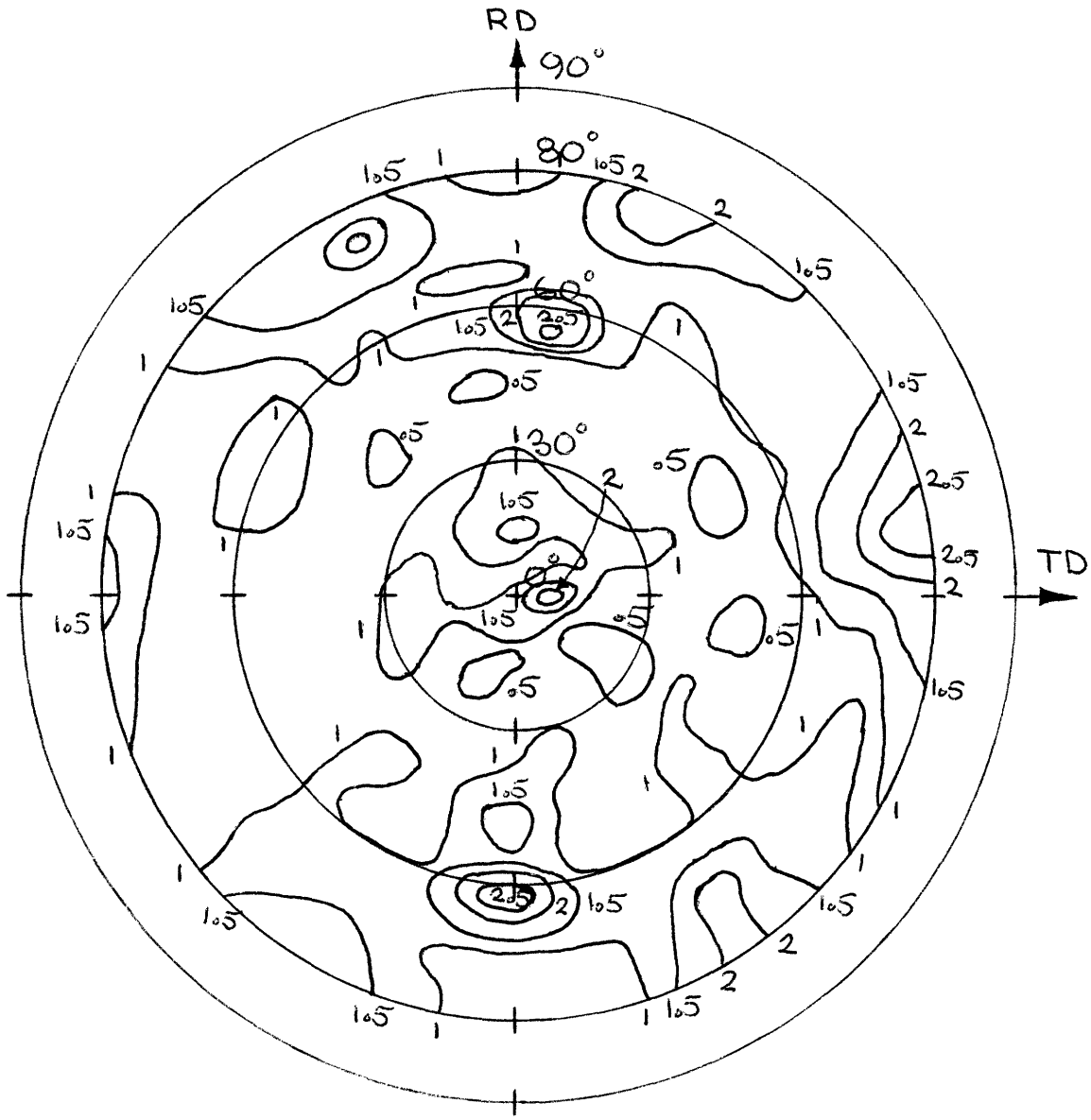

Figure 26 - Heat 225 Ferrite Phase Pole Figure ({110} Peak)

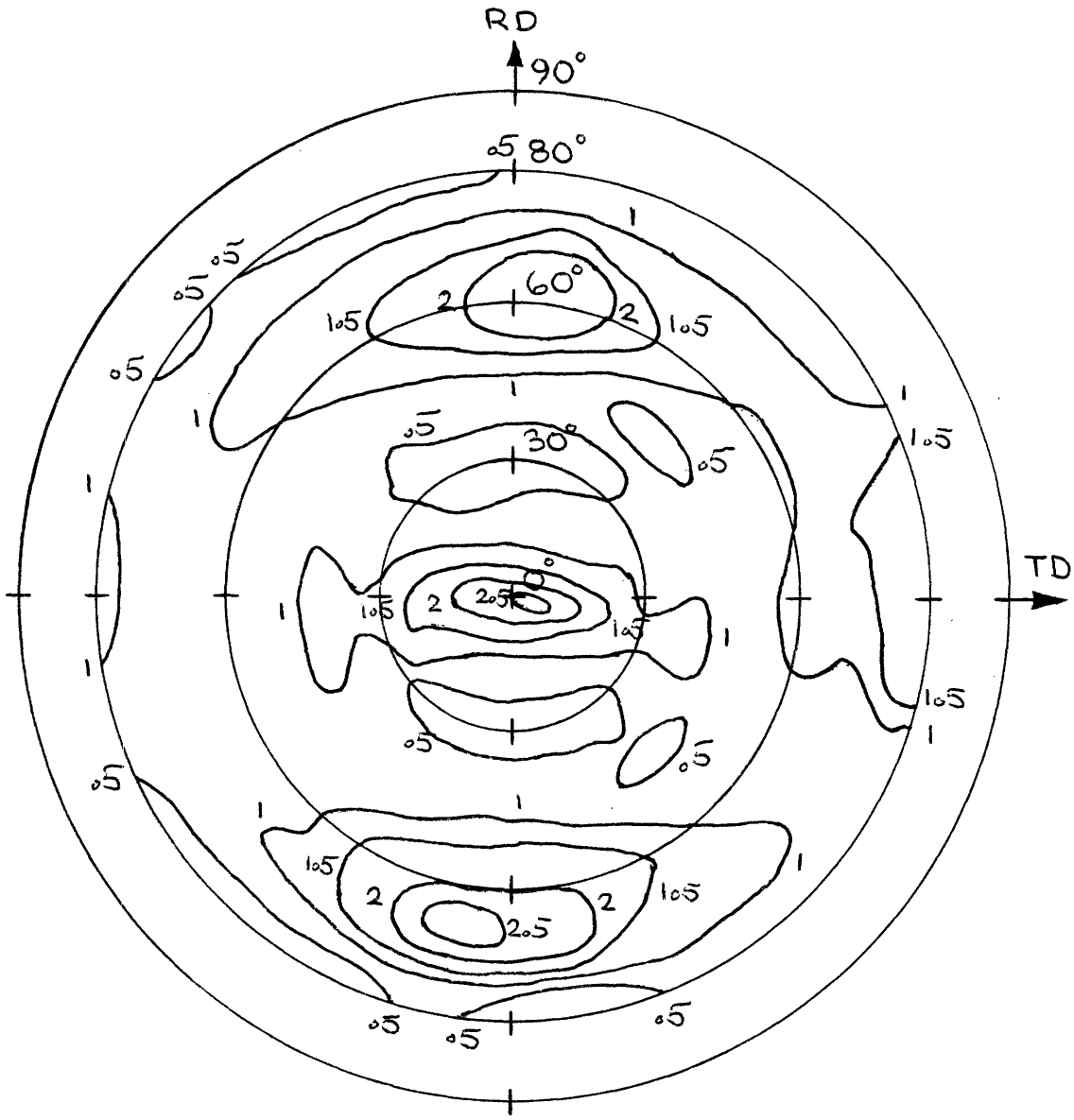

Figure 27 - Heat 225 Austenite Phase Pole Figure ({111} Peak)

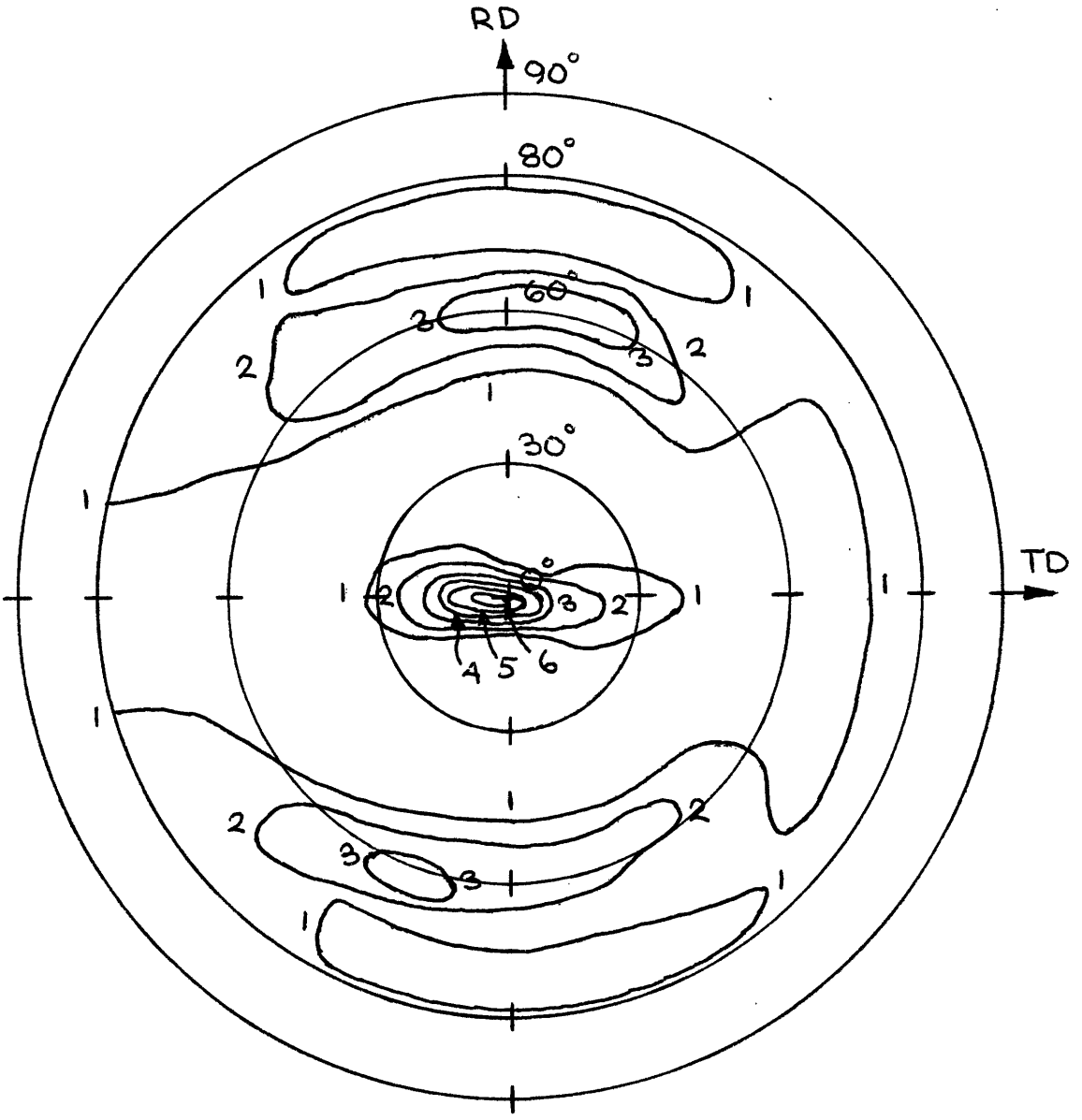

Figure 28 - Heat 226 Ferrite Phase Pole Figure ({110} Peak)

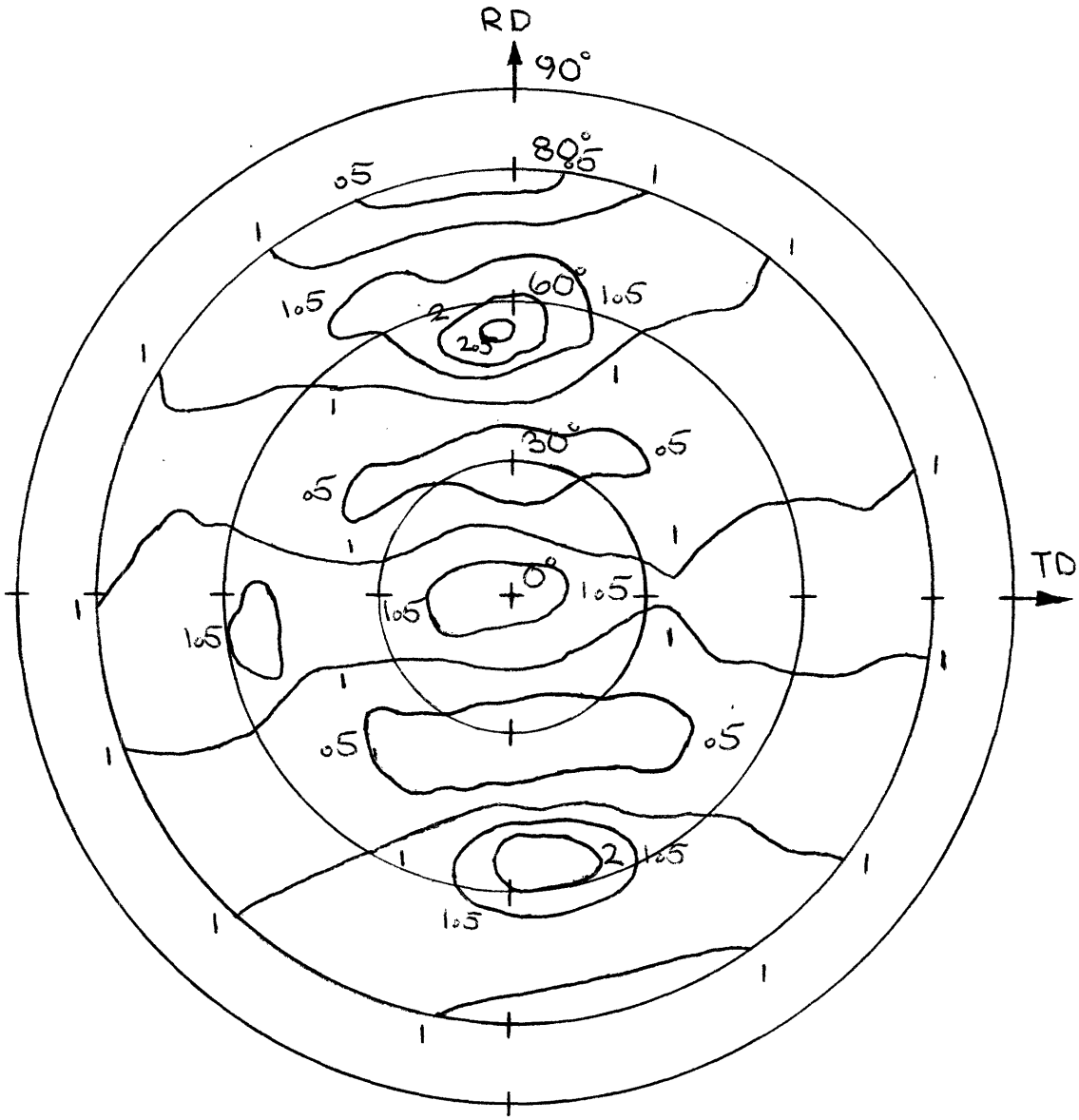

Figure 29 - Heat 226 Austenite Phase Pole Figure ({111} Peak)

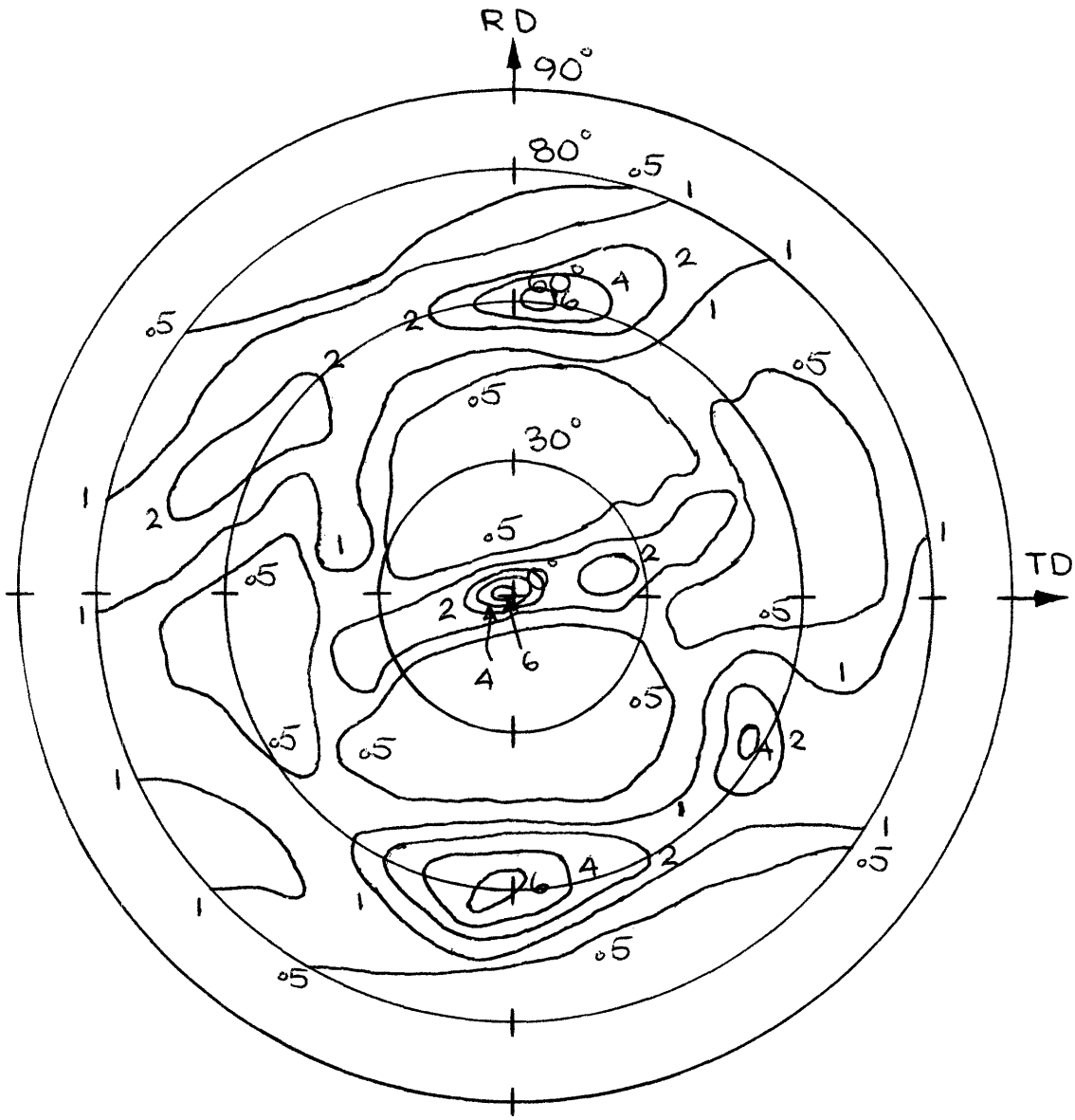

Figure 30 - Heat 227 Ferrite Phase Pole Figure ({110} Peak)

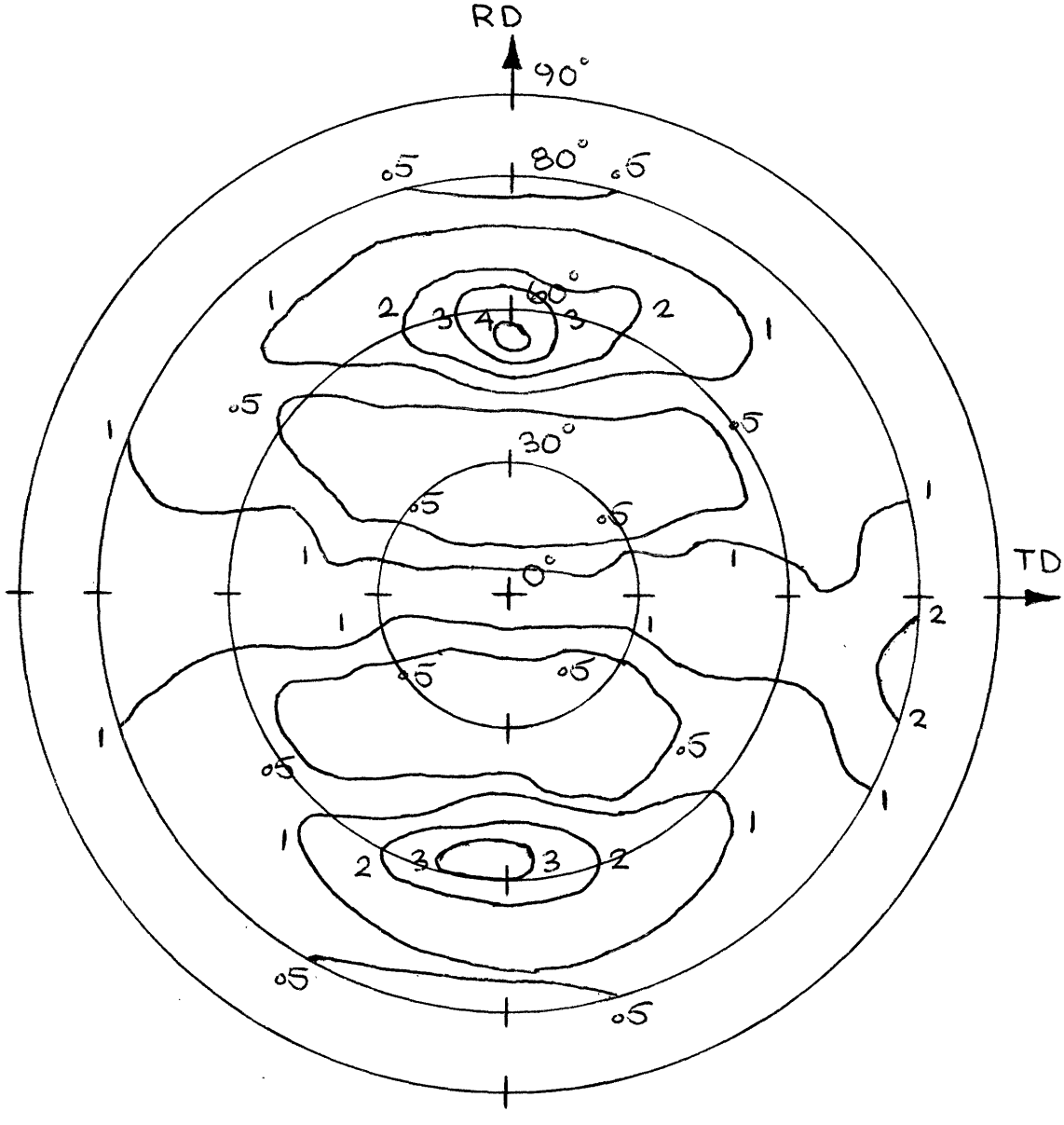

Figure 31 - Heat 227 Austenite Phase Pole Figure ({111} Peak)

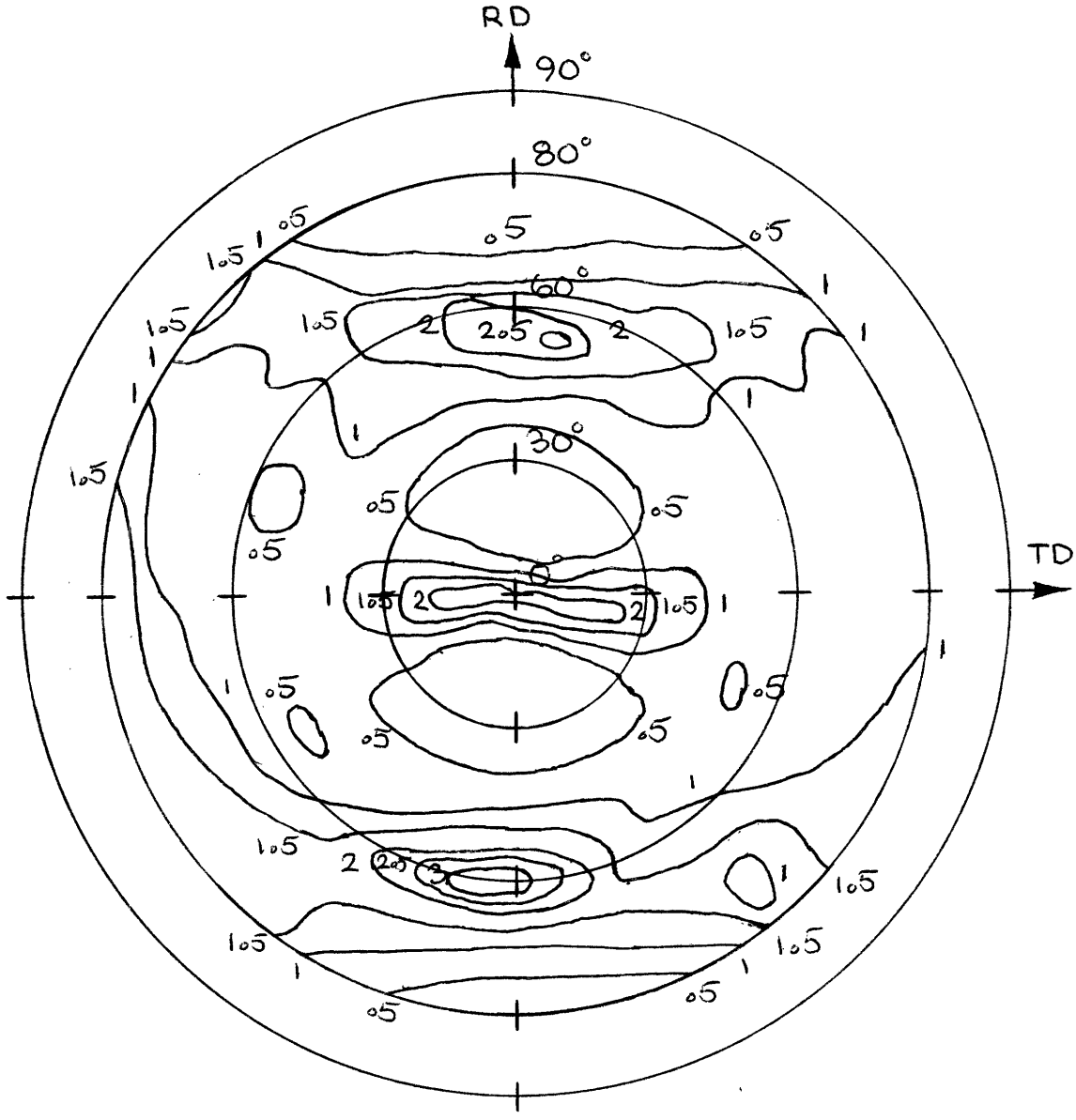

Figure 32 - Heat 229 Ferrite Phase Pole Figure ({110} Peak)

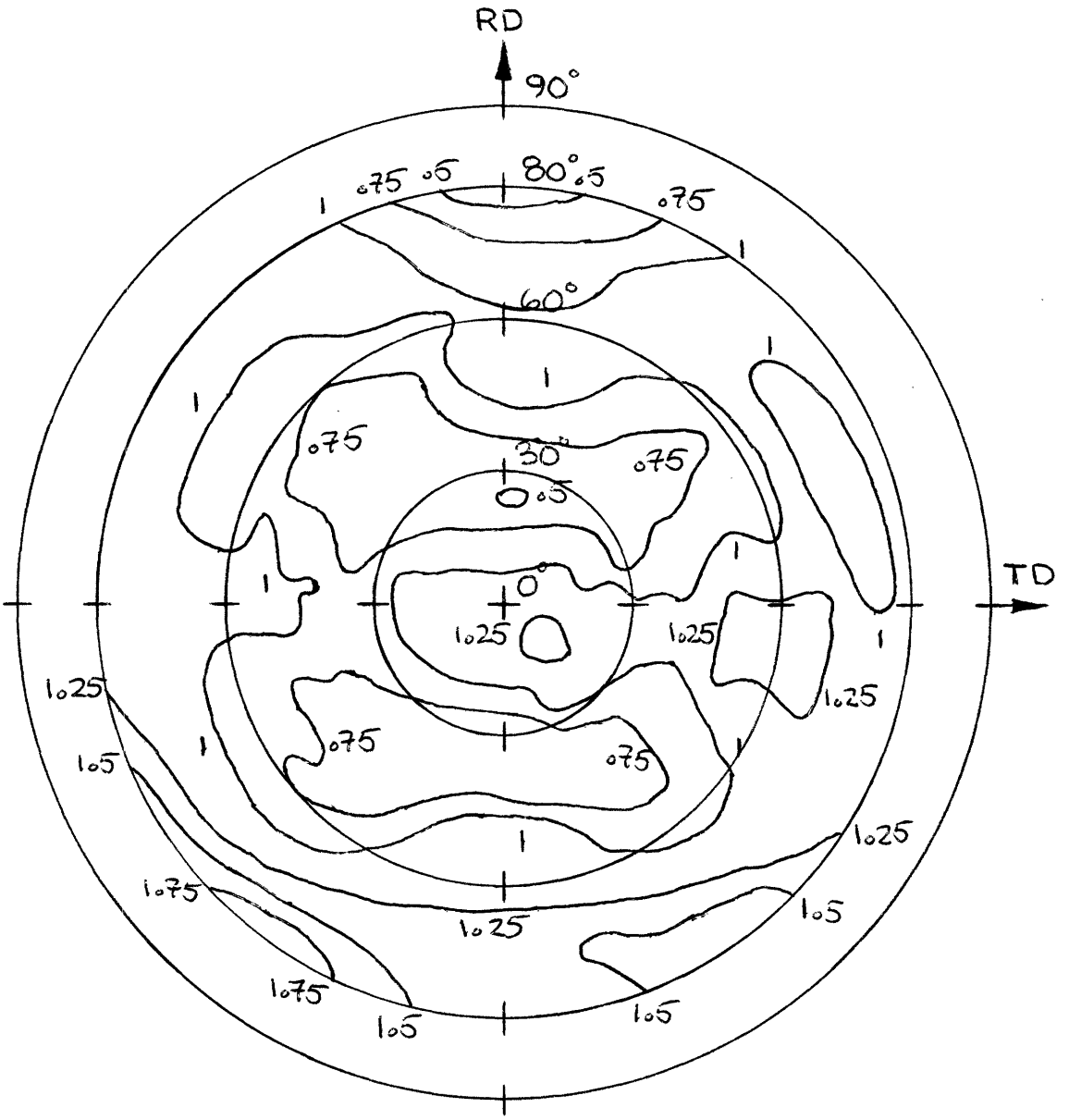

Figure 33 - Heat 229 Austenite Phase Pole Figure ({111} Peak)

imposed by the Kurdjumov-Sachs relationship should thus have a minimal effect on the hot rolling texture of the austenite phase of this alloy.

The characteristic features of the pole figure of these alloys are the strong intensity maxima at 50 to 70 degress to the plate normal in the rolling direction and, for the ferrite pole figures, at the plate normal. The pole figures seem to be the result of the superposition of independent textural components. With each intensity maximum is associated a ring of high intensity, at an angle which corresponds to that between families of planes in the crystal lattice under consideration (60° for the ferrite phase and 70.52° for the austenite phase). The intensity of this ring need not be constant around its circumference. As a result of the proximity of the angular spacings of the observed intensity maxima to that of families of planes in these crystals, overlap of the primary intensity maxima and the diffuse intensity rings is to be expected. For maxima aligned in the rolling direction, elongation of these regions in the transverse direction should occur and is observed. Thus, the observed pole figures can be well rationalized as being the superposition of independent textural components, each composed of an intensity maximum and an associated diffuse intensity ring.

V. CONCLUSIONS

1. Hot rolling of microduplex stainless steels brings about substantial mechanical orientation of the microstructures and pronounced and rather unusual crystallographic textures in the phases present.

2. The variation of indentation hardness with volume fraction of ferrite in this alloy series may be well explained as a superposition of two effects. The ferrite grain size refining effect of austenite additions to ferrite matrix alloys initially dominates the hardness behavior. With further austenite additions, the Law-of-Mixtures Strength relationship leads to somewhat lower hardness values.

3. The partitioning of the alloying elements is significant and in accord with thermodynamic predictions.

4. The variation of the fatigue crack initiation lifetimes of these alloys with volume fraction ferrite results both from the variation of yield stress and the ability of the microduplex structure to effectively disperse slip and delay crack initiation.

VI. SUGGESTIONS FOR FURTHER WORK

1. To study the development of crystallographic orientation in this two-phase alloy series. This would entail observing the effect of various rolling reductions on the textures of the austenite and ferrite phases.

2. To ascertain the relationship between the mechanical orientation developed during hot rolling of these alloys and the textures observed.

3. To more thoroughly characterize the process of slip dispersal by the microduplex alloys 225, 226 and 227.

4. To study the above phenomena for other two-phase alloy systems.

VII. REFERENCES

1. J. A. Moskovitz , Ph.D. Thesis, MIT, Cambridge, Mass. 1977.
2. S. Floreen and H. W. Hayden, ASM Trans. Q. 61 (1968), 489.
3. H. W. Hayden and S. Floreen, Met. Trans. 4 (1973), 651
4. M. Hansen and K. Anderko, Constitution of Binary Alloys, McGraw-Hill, New York, 1958.
5. R. P. Elliott, Constitution of Binary Alloys, First Supplement, McGraw-Hill, New York, 1965.
6. F. A. Shunk, Constitution of Binary Alloys, Second Supplement, McGraw-Hill, New York, 1969.
7. Metals Handbook, Volume 8, American Society for Metals, Metals Park, Ohio, 1973.
8. R. Lagneborg, ASM Trans. Q. 60 (1967), 67.
9. R. L. Cowan, Jr. and C. S. Tedmon, Jr., Intergranular Corrosion of Iron-Nickel-Chromium Alloys, General Electric CRD, Schenectady, New York, 1972, p. 7.
10. N. Yukawa, et al., Met. Trans., 3 (1972), 887.
11. N. Yukawa, et al., J. Jap. Inst. Metals, 35 (1971), 1100.
12. A. H. Sully, J. Inst. Metals, 80 (1951-52), 173.
13. P. A. Beck and W. D. Manly, Trans. AIME, 185 (1949), 354.
14. P. Schafmeister and R. Ergang, Arch. Eisenh., 12 (1938-39), 459.
15. A. T. Grigoriev and V. V. Kuprina, Russ. J. Inorg. Chem., 8 (1963) 1342.
16. A. T. Grigoriev and E. M. Sovolovskaya, Vestn. Mosk. Un-ta.: Khimiya, 2 (1961), No. 6, 3.

18. J. W. Pugh and J. D. Nisbet, Trans. AIME, 188 (1950), 268.

19. A. J. Cook and B. R. Brown, J. Iron Steel Inst., 171 (1952), 345.

20. B. Hattersley and W. Hume-Rothery, J. Iron Steel Inst., 204 (1966) 683.

21. J. W. Schultz and H. F. Merrick, Met. Trans., 3 (1972).

22. W. P. Rees, et al., J. Iron Steel Inst., 162 (1949), 325.

23. L. Kaufman and H. Nessor, Met. Trans., 5 (1974), 1617.

24. P. E. Price and N. J. Grant, Trans. AIME, 215 (1959), 635.

25. R. E. Lismer, et al., J. Iron Steel Inst., 171 (1952), 49.

26. G. Masing, Ternary Systems, Dover, New York, 1944, p. 79.

27. A. L. Schaeffler, Metal Progress, 56 (1949), 680.

28. L. Pryve and K. W. Andrews, J. Iron Steel Inst., 195 (1960), 415.

29. H. -J. Schuller and H. Henneke, Arch. Eisenh., 39 (1968), No. 11, 1.

30. H. W. Hayden and S. Floreen, ASM Trans. Q., 61 (1968), 474.

31. R. C. Gibson, et al., ASM Trans. Q., 61 (1968), 85.

32. F. Lecroisey and A. Pineau, Met. Trans., 3 (1972), 387.

33. C. S. Tedmon, Jr., and D. A. Vermilyea, Met. Trans., 1 (1970), 2043.

34. J. W. Flowers, et al., Corrosion, 19 (1963), 186t.

35. E. E. Underwood, Quantitative Stereology, Addison-Wesley, Reading, Mass., 1970, p. 15.

36. E. E. Underwood and E. A. Starke, Jr., ONR Contract NOOO14-75-C-0349 Technical Report 78-1.

37. ASTM Standard E81, American Society for Testing and Materials, Philadelphia, 1976.

38. G. E. Dieter, Mechanical Metallurgy, McGraw-Hill, New York, 1976, p. 394.

39. P. G. Shewmon, Transformations in Metals, McGraw-Hill, New York, 1969, p. 213.